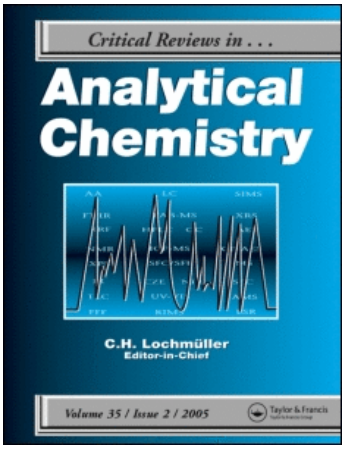

Critical Reviews in Analytical Chemistry
Publication details, including instructions for authors and subscription information:
http://www.informaworld.com/smpp/title~content=t713400837

Coherent Forward Scattering Spectroscopy (Cfs): Present Status and Future Perspectives

Gerd M. Hermann; Kay Niemax

To cite this Article Hermann, Gerd M. and Niemax, Kay(1988) 'Coherent Forward Scattering Spectroscopy (Cfs): Present Status and Future Perspectives', Critical Reviews in Analytical Chemistry, 19: 4, 323 — 377
To link to this Article: DOI: 10.1080/10408348808542814
URL: http://dx.doi.org/10.1080/10408348808542814

COHERENT FORWARD SCATTERING SPECTROSCOPY (CFS): PRESENT STATUS AND FUTURE PERSPECTIVES*

Author: **Gerd M. Hermann**
Department of Physics
Justus-Liebig Universitat
Giessen, Federal Republic of Germany

Referee: Kay Niemax
Institut fur Spektrochemie und Angewandte Spektroskopie (ISAS)
Dortmund, Federal Republic of Germany

I. INTRODUCTION

*Dedicated to Prof., Dr., Drs. h. c. Arthur Scharmann on the occasion of his 60th birthday, with the appreciation of his merits in the field of CFS.

A. Level-Crossing Phenomena and the Effect of Coherent Forward Scattering

Coherent forward scattering (CFS — used for the physical effect as well as for the approach of coherent forward scattering spectroscopy) has been investigated first in connection with atomic resonance radiation phenomena like double resonance and level-crossing effects.[1] The very early level crossing has been measured in lateral fluorescence in a weak magnetic field.[2] This "zero-field level crossing" in lateral detected resonance fluorescence is called "Hanle effect"[3] and can be classically described by the model of an atomic oscillator, emitting during its Larmor precession with respect to the applied magnetic field (Figure 1).

In lateral fluorescence, differences of optical paths of excitation and detection are large compared with the optical wavelength (Figure 2a). Thus, only coherences of Zeeman sublevels of the excited state of the same individual atom contribute to the coherence of counterpolarized linear or circular components and, thus, to polarization of fluorescence light. Zeeman coherences are generated with polarized light by coherent excitation of different magnetic sublevels, which overlap within their natural width (Figure 3).

By variation of the magnetic field applied in a configuration, as shown in Figure 4, the direction and the degree of polarization is changed by variation of the degree of overlapping of excited Zeeman levels. The typical Hanle curve, representing the degree of polarization as a function of a weak magnetic field (zero-field level crossing), as well as the intensities of light polarized parallel and perpendicular with respect to the incident polarization, are given in Figure 5. The plane of the mean polarization is also rotated. The direction as well as the degree of polarization can be derived from Hanle's classical model by averaging the emitted light with respect to the directions of the preceding oscillator. Level-crossing measurements are an efficient tool for determination of atomic lifetimes, collisional depolarization cross sections and hyperfine structures, as well as for measurement of weak magnetic fields (e.g., in the solar preminescences).[4]

In forward direction, all optical paths from the source via atomic interaction to the detector are equal (Figure 2b). Thus, all optically induced dipole oscillations of resonant atoms contribute coherently to the detected radiation. As shown below, the optical interaction can be described by a macroscopic polarizability of the atomic vapor. This macroscopic description is equivalent to a description by the complex refractive index.[1] Due to the coherent anisotropic interaction, the polarization of light is changed by linear or circular dichroism and birefringence. Thus, by a polarizer configuration, as shown in Figure 6, in the limit of

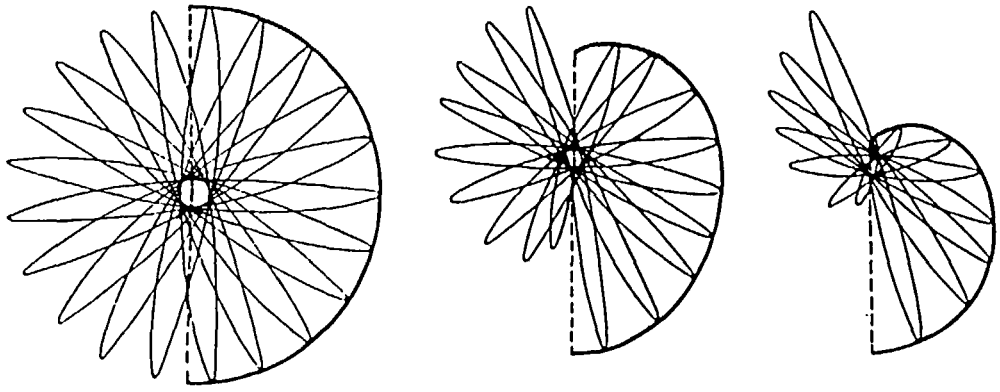

FIGURE 1. Hanle's oscillator model of atomic emission in an external magnetic field.[2]

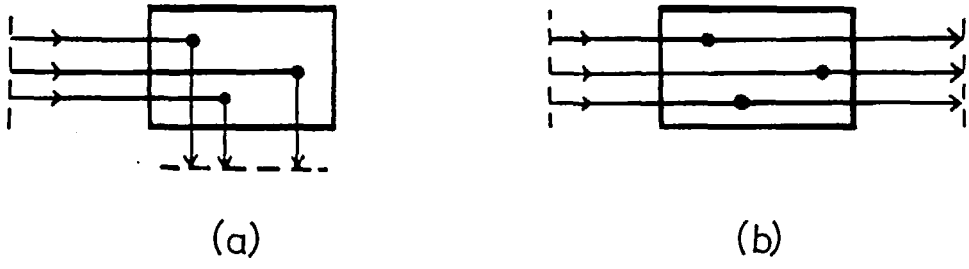

FIGURE 2. (a) Random optical paths in lateral fluorescence. (b) Equal optical paths in CFS.[14]

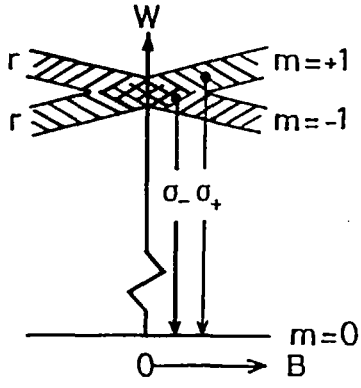

FIGURE 3. Crossing of Zeeman levels of finite width Γ.[4]

a pure dispersive interaction, the total incident light intensity can be transmitted without loss.

Due to the Doppler effect, caused by the atomic velocity distribution, the damping of the macroscopic coherent polarization as well as the widths of the crossing profiles are related to the width of the corresponding plasma dispersion function (Section IV.B). Applications of this crossing effect[5,6] are not restricted to crossing levels of the same atomic species only, but also occur with crossing lines of different atomic species, i.e., of different isotopes.[7,8] The term "line crossing" which has been proposed for these effects[5] is used by some authors

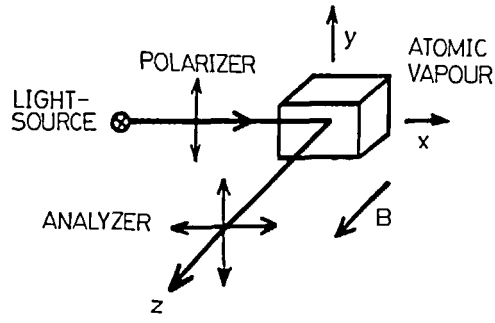

FIGURE 4. Experimental configuration for the Hanle-effect measurement.[4]

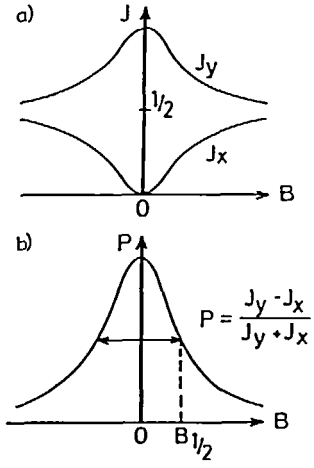

FIGURE 5. "Hanle curves": (a) Lateral fluorescence intensities J_y and J_x polarized parallel and perpendicular with respect to polarization of the incident light. (b) Degree of polarization in lateral fluorescence as a function of an external magnetic field.[4]

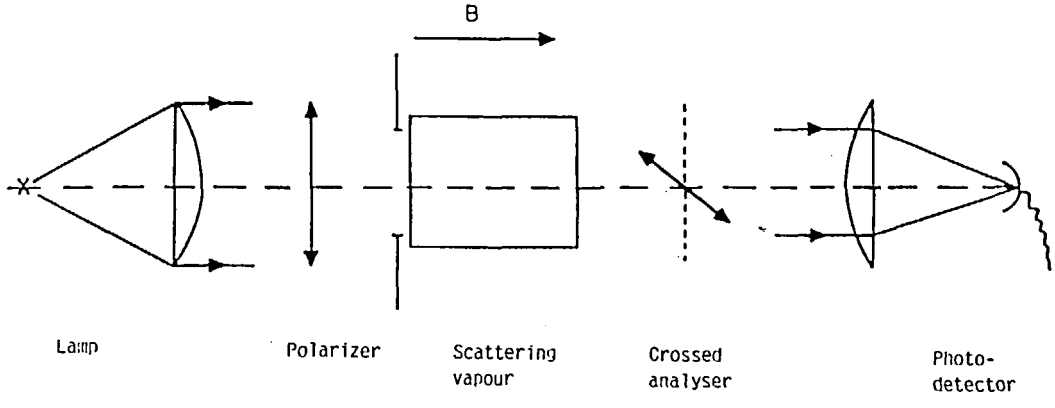

FIGURE 6. Experimental arrangement for CFS in Faraday configuration.[5]

with restriction to line crossing of different isotopic species only. Other authors follow this proposal and use "line crossing" for all effects that are related to macroscopic coherent interactions of light with an ensemble of different individual atoms in the spectral range of their crossing lines, whether or not they are of the same isotopic species (see also Section IV.B). The latter notation, which is consequently used in this paper, includes effects that are also called "Doppler-broadened level-crossing effects".

Experimental performances for line-crossing measurements, as show typically in Figure 6, use longitudinal magnetic fields (Faraday configuration) as well as transverse fields (Voigt configuration). The shape of the line-crossing signal for low atomic density ("weak scattering limit"[1]) allows the determination of the width of the Gaussian Doppler line at low buffer gas pressure[5] or its Lorentzian profile at atmospheric pressure.[9] Hyperfine structures have been measured by hyperfine line crossings[7] as well as isotope shifts by isotopic line crossings.[10]

At higher atomic densities, when phase retardations attain unity order of magnitude, the line crossing becomes narrower (coherence narrowing). At a very high atomic density, when resonant light is absorbed on a pathlength, shorter than the optical wavelength, path differences in reflection are short compared with the wavelength, and interference becomes coherent in the backscattering direction. Thus, macroscopic coherence is relevant again in "selective reflection" with similar line-crossing effects as known from CFS.[8] Hanle and Stanzel[11] measured the first zero-field line crossing in selective reflection. Hanle, Scharmann, Schnaar, Siegmund,[12] determined the related isotope shift by means of the line-crossing profile of the isotopes Hg 200 and Hg 202 in selective reflection.

The principle of CFS is also well known as polarization spectroscopy and frequently applied in laser spectroscopy.[13] It allows the sensitive detection of changes of phases or intensities of counterpolarized components of light by weak atomic interaction, whether by absorption or dispersion. With intensive radiation fields of lasers, saturation-induced Doppler-free[14-16] level-crossing and mode-crossing[17] signals can be observed in forward direction as well as Doppler-broadened phenomena due to the linear atomic resonance interaction.

B. Analytical Application of CFS

Zeeman scanning of atomic resonance lines has been applied very early in atomic absorption and fluorescence technique to measure atomic lines and line profiles.[18-20] A very important application of magnetic line scanning is background compensation in direct or inverse Zeeman atomic absorption spectroscopy (ZAAS).[21,22] The first investigations using CFS for trace element detection of mercury have been carried out by Hadeishi.[23,24] A heated sample cell in longitudinal magnetic field (Faraday configuration) has been employed with a line source (containing Hg 198 or Hg 204 single isotope), which could also be tuned by a longitudinal magnetic field. It could be shown that Hg concentrations in the range of ppb ($\mu g/m^3$) are detectable.

In combination with hollow-cathode lamps and electrothermal atomization (ETA), especially with graphite furnaces (GF-ETA), CFS has been found very sensitive for determination of trace elements.[25] Nevertheless, the greatest advantage of CFS is the option of real multielement determination in simultaneous or sequential operation with continuum spectrum light sources.[26-29]

Today, atomic absorption spectroscopy (AAS) is a very powerful tool with not very high demands on the optical detection channel. But despite some available multielement lamps, it is still a method for single-element determination. Optical emission spectroscopy (OES) has become a highly performed technique, too, especially in combination with inductively coupled plasmas (ICP). However, due to the extensive spectra with many ion lines and lines of higher excited states, OES requires much higher spectral resolution than techniques of atomic resonance spectroscopy. Furthermore, OES is almost restricted to flames and plasmas as analytical sources. Thus, there is increasing demand for atomization-independent optical spectroscopic real multielement detection methods.

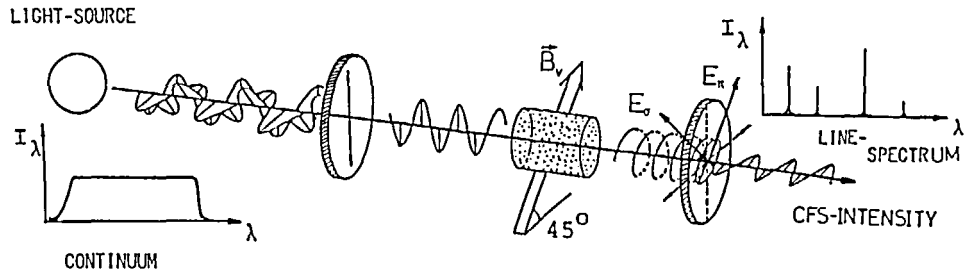

FIGURE 7. Principle of CFS with a Voigt configuration and a continuum source.[44]

For that purpose, valuable work has been done on detection of weak intensities from thermal emission in graphite furnaces,[31] on development of furnace atomization nonthermal excitation spectroscopy (FANES),[31] and on simultaneous multielement determination by AAS with continuum spectrum sources (SIMAC).[32,33] However, the SIMAC technique requires high spectral resolution of a large spectrograph, and calibration depends on the convolution of the detected spectral window with the atomic resonance line profile and thereby offers the opportunity of an extreme expansion of the dynamic range to higher concentrations by wavelength adjustment to the furthest wings of the absorption lines.

Nevertheless, as shown in the following, CFS in combination with continuum spectrum light sources presents interesting perspectives as an optical resonance interaction approach for simultaneous and sequential multielement determination.

II. MEASUREMENT OF ANISOTROPIC ATOMIC RESONANCE INTERACTION BY CFS

A. The Principle and Basic Arrangement

The principle of coherent forward-scattering spectroscopy is shown in Figure 7. The analyte is vaporized in between two crossed polarizers. The lamp may be a continuum spectrum or an atomic line source. Without anisotropic interaction, the light path is blocked by the crossed polarizers. Due to the applied longitudinal (Faraday configuration) or transverse magnetic field (Voigt configuration), the atomic resonance lines split up into σ and π components (Figure 8). The π components are polarized parallel with respect to the applied magnetic field, while the polarization of σ components is perpendicular to the field with a circular or linear state, depending on the direction of propagation parallel or perpendicular with respect to the magnetic field. Figure 8 shows the Zeeman structure of a Lorentzian triplet in the case of the normal Zeeman effect of a singlet transition line.

Caused by the magnetically induced anisotropy, polarization of the incident light is changed in the spectral range of atomic resonance lines, and the resonance spectrum of the analyte vapor is transmitted. CFS is a zero method. Under ideal conditions, the detected intensity is zero for zero atomic resonance interaction. Under constant remainder parameters, the intensity of a line, transmitted by CFS, depends only on the atomic analyte vapor density. The CFS spectrum is recorded by a monochromator in combination with a photomultiplier or simultaneously by a polychromator in combination with a vidicon, as demonstrated by Wirz, Debus, Hanle, and Scharmann,[34] or intensified by a channel plate with a diode array[29] (Section V.C.2).

B. Theory

In their very early work, Corney et al.[1] studied CFS with reference to double-resonance and level-crossing experiments. In a very general form, the authors discuss the interaction

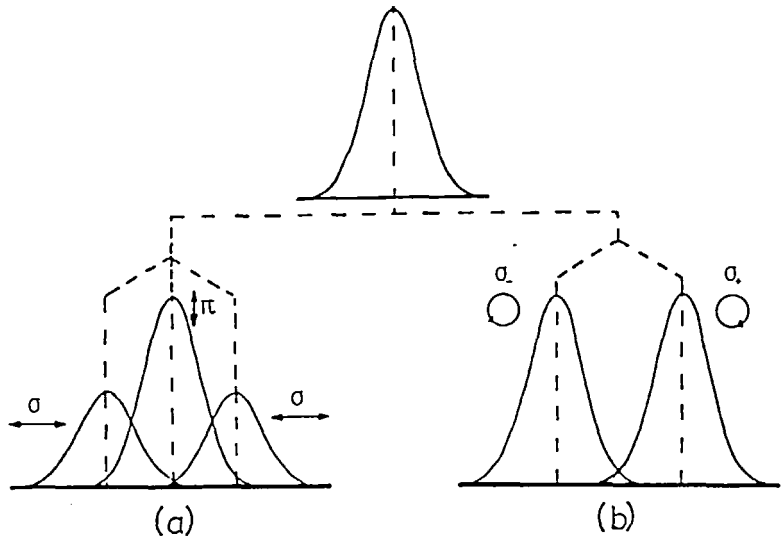

FIGURE 8. Line structure and polarization due to normal Zeeman effect in transverse (a) and longitudinal (b) direction.[35]

of polarized light with an atomic vapor in a static magnetic field combined with a perpendicular r.f. magnetic field. Their theoretical and experimental analyses include statis transverse and longitudinal fields. Later on, detailed discussions of the effect of CFS with Faraday and Voigt configurations, by use of line sources and continuum spectrum sources, and for different experimental layout, were published.[6-12,35,36] In the following, a short theoretical formulation of an anisotropic optical resonance interaction is given.

The macroscopic coherent resonance interaction can be described by a dielectric tensor ϵ or by the susceptibility tensor χ:

$$\epsilon = 1 + \chi \quad \text{with} \quad \chi = (\chi_{ij}) \tag{1}$$

and with the polarization:

$$\mathbf{P} = \epsilon_o \chi \mathbf{E} \tag{2}$$

By use of the common notation with the basic vectors e_q ($q = -1, 0, +1$):

$$\mathbf{e}_+ = (1/\sqrt{2})(\mathbf{e}_1 + i\mathbf{e}_2)\ \mathbf{e}_- = (1/\sqrt{2})(\mathbf{e}_1 - i\mathbf{e}_2) \qquad \mathbf{e}_o = \mathbf{e}_3 \tag{3}$$

and with the components of the electric field E_q:

$$E_+\mathbf{e}_+ = (1/\sqrt{2})(E_1\mathbf{e}_1 + iE_2\mathbf{e}_2)\ E_-\mathbf{e}_- = (1/\sqrt{2})(E_1\mathbf{e}_1 - iE_2\mathbf{e}_2) \qquad \mathbf{E}_o = \mathbf{E}_3 \tag{4}$$

(χ_{pq}) is diagonal if E_o is chosen parallel to the external magnetic field B ($e_o \parallel B$):

$$(\chi_{pq}) = \begin{pmatrix} \chi_-, & 0, & 0 \\ 0, & \chi_o, & 0 \\ 0, & 0, & \chi_+ \end{pmatrix} = (\chi_p \cdot \delta_{pq}) \tag{5}$$

The susceptibility is then represented by the three components χ_-, χ_o, χ_+.

Light propagating from the light source through the atomic vapor is given by the electrical vector E(z,t):

$$\mathbf{E}(z, t) = \sum_q \mathbf{e}_q \cdot E_q(z, t) = \sum_q \int \mathbf{e}_q \cdot E_q(k_q) \cdot \exp[i(k_q z - c_q k_q \cdot t)]\, dk \tag{6}$$

This follows Maxwell-d'Alembert's equation (c = velocity of light):

$$\Delta E - (1/c^2)(\partial^2/\partial t^2)\epsilon E = 0 \tag{7}$$

$$c_q^2 = c^2/n_q^2 = c^2/\epsilon_q = c^2/(1 + \chi_q) \tag{8}$$

$$\Delta E_q - (1/c^2)(\partial^2/\partial t^2)\epsilon_q E_q = \Delta E_q - (1/c^2)(\partial^2/\partial t^2)(1 + \chi_q)E_q = 0$$
$$= \Delta E_q - (n_q^2/c^2)(\partial^2/\partial t^2)E_q = 0 \tag{9}$$

At low optical densities (e.g., for gases), the approximation:

$$n_q = \sqrt{\epsilon_q} = \sqrt{(1 + \chi_q)} = 1 + \chi_q/2 \tag{10}$$

is valid. The electric susceptibility χ_q is given by the atomic polarizability(α_q) and the atomic number density n_A:

$$\chi_q = n_A\langle p_q\rangle/\epsilon_o E_q = n_A\langle\alpha_q\rangle/\epsilon_o \tag{11}$$

The polarizability (α_q) and the expectation value of the atomic electric dipole momentum $\langle\mathbf{p}\rangle$ can be calculated by first-order perturbation theory:[37]

$$\langle p_q\rangle = \alpha_q E_q = \langle s|p_q|s\rangle = e e_q\langle s|r|s\rangle \tag{12}$$

$|s\rangle = \Sigma c(k,m)|k,m_k\rangle$ represents the atomic state, which has no parity, in consequence of the perturbation by the radiation field. It follows the Schrödinger's equation:

$$i\hbar(d/dt)|s\rangle = H|s\rangle \tag{13}$$

with the Hamiltonian $H = H_o + V$. H_o describes the undisturbed atom with the eigenstates $|i, m_i\rangle$ and the energies E_{im} given by the time-independent Schrödinger equation $H_o|i,m_i\rangle = E_{im}|i,m_i\rangle$. The perturbation energy due to the radiation field $V = \mathbf{pE} = \mathbf{erE}$ can be written with the matrix elements $V_{ij} = \langle i|V|j\rangle = \langle i|\mathbf{erE}|j\rangle = \langle i|\mathbf{Ep}|j\rangle$. In absence of atomic collisions, the damping constant Γ_{ij} of the optical coherence between the states $|i\rangle$ and $|j\rangle$ is related to the lifetimes τ_i,τ_j of the atomic states with $2\Gamma_{ij} = (1/\tau) + (1/\tau_j)$. The state polarized by interaction with the propagating light is given by

$$|g'\rangle = |g\rangle + \sum_{i\mu jm} \frac{\langle i, \mu_i|V|j, m_j\rangle\langle j, m_j|g\rangle}{\hbar(\omega_{gm,i\mu} - \omega - i\Gamma_{ij})} |i, \mu_i\rangle \tag{14}$$

$$\alpha_q(g, m) = \langle p_q\rangle/E_q = \langle g'|p_q|g'\rangle/E_q$$
$$= \sum_{\substack{i,j,k \\ \mu_i m_j m_k}} 2\, \frac{\langle g|k, m_k\rangle\langle j, m_j|g\rangle\langle k, m_k|p_q|i, \mu_i\rangle\langle i, \mu_i|p_q|j, m_j\rangle}{E_q \cdot \hbar(\omega_{gm,i\mu} - \omega - i\Gamma_{ij})}\, \delta_{\mu,m+q} \tag{15}$$

Since off-resonant contributions can be neglected, only the polarization of the initial ground-state level |g,m>, in interaction with the resonant excited levels |e,m'>, has to be taken into account:

$$\alpha_q(g, m) = (p_q)/E_q = \sum_{m'} \frac{2|\langle e, m'|p_q|g, m\rangle|^2}{\hbar(\omega_{mm'} - \omega - i\Gamma)} \delta_{m',m+q} \tag{16}$$

Using Wigner-Eckart's theorem[37] and the reduced dipole matrix element <g||p||e>, we find:

$$\alpha_q(g, m) = \frac{2\begin{pmatrix} J & J' & 1 \\ m & q - m & -q \end{pmatrix}^2 \langle e||p||g\rangle|^2}{\hbar(\omega_{mm'} - \omega - i\Gamma)} \tag{17}$$

With the sum rule[37] for Wigner's 3 − j symbols:[38]

$$\Xi(JJ') = \sum_q \begin{pmatrix} J & J' & 1 \\ m & q - m & -q \end{pmatrix}^2 = \begin{cases} (J + 1)(2J + 3) & \text{for } J' = J + 1 \\ J(J + 1) & J' = J \\ J(2J - 1) & J' = J - 1 \end{cases} \tag{18}$$

and the oscillator strength f(J',J) = f(eJ',gJ)

$$f(J'J) = \frac{2m\omega}{3e^2\hbar} \sum_{m'} |\langle em'|p|gm\rangle|^2 \tag{19}$$

$$= \frac{2m\omega}{3e^2\hbar} |\langle e||p||g\rangle|^2 \sum_q \begin{pmatrix} J & J' & 1 \\ m & q - m & -q \end{pmatrix}^2$$

$$= \Xi(JJ') \frac{2m\omega}{3e^2\hbar} |\langle e||p||g\rangle|^2 \tag{20}$$

the polarizability of the ground-state level |g,m> with the component α_q related to the polarization vector e_q results as

$$\alpha_q(g, m, \omega_{m,m+q} - \omega) = \frac{3e^2 f(eJ', gJ)\begin{pmatrix} J & J' & 1 \\ m & q - m & -q \end{pmatrix}^2}{m\omega_{mm'} \cdot \Xi(JJ')(\omega_{mm'} - \omega - i\Gamma)} \tag{21}$$

If the ground state is unpolarized (no optical pumping, i.e., at low optical intensity), the population of all magnetic sublevels $n_A(g,m) = n_A(g)/(2J + 1)$ is equal. With the sum rule complementary to Equation 18:

$$\sum_m \begin{pmatrix} J & J' & 1 \\ m & q - m & -q \end{pmatrix}^2 = (2J + 1) \cdot \Xi(JJ')/3 \tag{22}$$

and for dipole transitions we find the susceptibility of the isotropic vapor as

$$\chi = \sum_m \alpha(g, m) n_A/\epsilon_o(2J + 1) = (e^2/\epsilon_o m\omega_{g,e}) n_A f(e, g)/(\omega_{e,g} - \omega - i\Gamma) \tag{23}$$

which is in agreement with the classical model.[39]

Due to the Doppler effect in combination with the Gaussian atomic velocity distribution, the susceptibility is represented by a Voigt profile:

$$\chi_q(\omega) = n_A/(\sqrt{\pi}(2J + 1)\Delta\epsilon_o) \sum_m \int \alpha_q(g, m, \omega_{m,m+q} - \omega + u)\exp(-u^2/\Delta^2)\, du \quad (24)$$

$$= \frac{n_A\, 3e^2\, f(eJ', gJ)/\epsilon_o}{(2J + 1)\sqrt{\pi}\Delta\omega_{e,g} \cdot \Xi(JJ')} \sum_m \begin{pmatrix} J & J' & 1 \\ m & q - m & -q \end{pmatrix}^2 \cdot$$

$$\cdot \int \exp(-u^2/\Delta^2)/(\omega_{m,m+q} - \omega + u - i\Gamma)\, du \quad (25)$$

$$= \frac{n_A\, 3e^2 \cdot f(eJ', gJ)}{(2J + 1) \cdot \Delta\epsilon_o m\omega_{g,e} \cdot \Xi(JJ')} \sum_m \begin{pmatrix} J & J' & 1 \\ m & q - m & -q \end{pmatrix}^2 Z(x_{m,m+q} + iy) \quad (26)$$

with $\omega_o = \omega_{e,g}$; $X_{m,m+q} = (\omega - \omega_{m,m+q})/\Delta$; $y = \Gamma/\Delta$ and

$$Z(x + iy) = (1/\sqrt{\pi}) \int_{-\infty}^{+\infty} \exp(-t^2)/(u - x - iy)\, du \quad (27)$$

$Z(x + iy)$ is the plasma dispersion function[40] with the full half-width of Doppler broadening: $2\sqrt{\ln 2} \cdot \Delta = 2\omega_o\sqrt{(\ln 2 \cdot k_B T/M_A c^2)}$, where T = temperature, k_B = Boltzmann's constant, M_A = atomic mass, and c = velocity of light. Using the definition of Z_q given in Equation 28, Equation 26 is reduced to Equation 29:

$$Z_q[(\omega - \omega_{e,g} + i\Gamma)/\Delta] = \frac{1}{(2J + 1) \cdot \Xi(J, J')} \sum_m \begin{pmatrix} J & J' & 1 \\ m & q - m & -q \end{pmatrix}^2 \cdot$$

$$\cdot Z[(\omega - \omega_{m,m'+g} + i\Gamma)/\Delta] \quad (28)$$

$$\chi_q(\omega) = \frac{n_A\, 3e^2\, f(eJ', gJ)}{\Delta\, \epsilon_o\, m\, \omega_{g,e}} Z_q[(\omega - \omega_{g,e} + i\Gamma)/\Delta] \quad (29)$$

In an external magnetic field $B_o = B_o \cdot e_o$, the energy levels E_i split up by the Zeeman effect into the magnetic sublevels ($E_{im} = E_i + m \cdot g_i(e\hbar/2m)B_o = E_i + m \cdot g_i\gamma B_o$, $\mu_B = e\hbar/2m$ = Bohr's magneton, g_i = Landé's factor, $\gamma = g \cdot \mu_B/\hbar = g \cdot e/2m$ = gyromagnetic ratio). Consequently, the resonance frequencies are

$$\omega_{gm,em'} = \omega_{m,m'} = \omega_{m,m+q} = (E_e - E_g)/\hbar + (m'g_e - mg_g)(e/2m)B_o$$

$$= \omega_o + ((m + q)g_e - mg_g)(e/2m)B_o = \omega_o + (m(g_e - g_g) + qg_e)(e/2m)B_o \quad (30)$$

The complex refractive index $n_q = n_q' + in_q''$ follows Equation 10:

$$n_q = \sqrt{(1 + \chi_q)} = 1 + \chi_q/2$$

$$= 1 + [n_A\, 3e^2\, f(eJ', gJ)/(2\Delta\epsilon_o m\omega_o)]\, Z_q[(\omega - \omega_o + i\Gamma)/\Delta] \quad (31)$$

and can be expressed by the generalized form of the frequently used combinations:

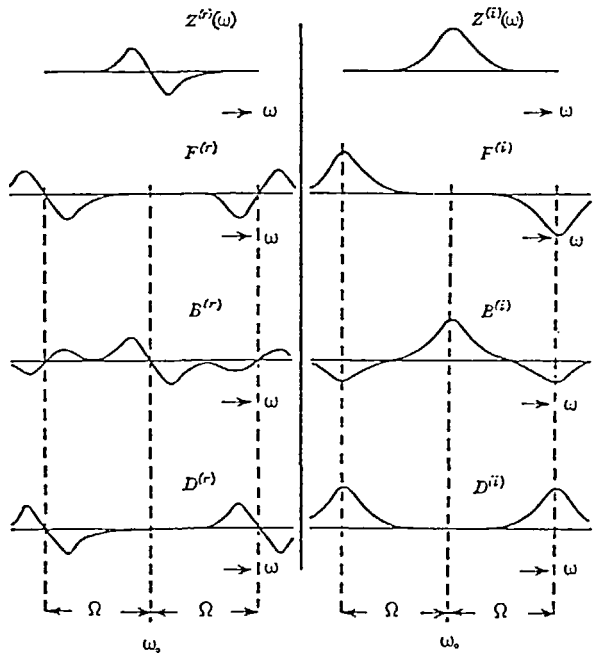

FIGURE 9. Qualitative profiles of the real and imaginary part of the plasma dispersion function $Z(\omega - \omega_o)$, without magnetic field and of the Faraday function $F(\omega - \omega_o)$, the birefringence function $B(\omega - \omega_o)$, and mean dispersion function $D(\omega - \omega_o)$ (normal Zeeman effect, $\Omega = \gamma \cdot B_o$ = Larmor frequency).[1]

$$F(\omega) = Z_+[(\omega - \omega_o + i\Gamma)/\Delta] - Z_-[(\omega - \omega_o + i\Gamma)/\Delta] \quad \text{(Faraday function)}$$

$$D(\omega) = Z_+[(\omega - \omega_o + i\Gamma)/\Delta] + Z_-[(\omega - \omega_o + i\Gamma)/\Delta] \quad \text{(mean dispersion function)}$$

$$B(\omega) = Z_o[(\omega - \omega_o + i\Gamma)/\Delta] - (1/2) \cdot D \quad \text{(birefringence function)} \qquad (32)$$

Due to Equations 28 and 29 in this formulation the factor $1/\Xi$ is already included in Z_q and thereby in $F(\omega)$, $B(\omega) = \Sigma\, a_q \cdot Z_q$ (with $a_q = -1, 0, +1$ for the Faraday configurations or $a_q = 1/2, -1, 1/2$ for the Voigt configurations).

In this notation, a longitudinal field (Faraday configuration) with B_o and e_o parallel to the z direction of light propagation) causes circular birefringence (Faraday effect) and circular dichroism, both described by $\Delta n_F = \Sigma a_q n_q$. The total absorption is described by the mean index n_F (complex representation $n = n' + in''$):

$$\Delta n_F = n_+ - n_- = (3n_A e^2 f)/(2\Delta\, \epsilon_o m\omega_o)F(\omega)$$

$$n_F = (n_+ + n_-)/2 = (3n_A e^2 f)/(4\Delta\, \epsilon_o m\omega_o)D(\omega) \qquad (33)$$

A transverse magnetic field (Voigt configuration with B_o and e_o perpendicular to the z direction of propagation) results in linear birefringence and dichroism given by

$$\Delta n_v = n_\pi - n_\sigma = [(3n_A e^2 f)/(2\Delta\, \epsilon_o m\omega_o)]B(\omega)$$

$$n_v = (n_\pi + n_\sigma)/2 = [(3n_A e^2 f)/(4\Delta\, \epsilon_o m\omega_o)][Z_o(\omega) + D(\omega)/2] \qquad (34)$$

Typical profiles of the real and imaginary part of $Z(\omega)$, representing the dispersion without magnetic field, and the functions $F(\omega,B_o)$, $B(\omega,B_o)$, and $D(\omega,B_o)$ are shown in Figure 9.

$$n''(\omega) = -\frac{1}{\pi}\int_0^\infty \frac{n'(x) - 1}{x - \omega}\,dx \qquad (n'(\omega) - 1) = \frac{1}{\pi}\int_0^\infty \frac{n''(x)}{x - \omega}\,dx \quad (43\text{–}44)$$

Those relations represent Cauchy's integral theorem applied to the complex dispersion $n(\omega) - 1 = n'(\omega) - 1 + i{\cdot}n''(\omega)$. The same integral theorem can also be applied to any difference of refractive indexes $\delta n(\omega) = \Sigma a_q n_q(\omega)$ as the birefringence function $F(\omega)$ ($a_q = -1/2, 1, -1/2$) or the Faraday function $F(\omega)$ ($a_q = -1, 0, +1$):

$$\delta n'(\omega) = \frac{1}{\pi}\int_0^\infty \frac{\delta n''(x)}{x - \omega}\,dx \qquad \delta n''(\omega) = -\frac{1}{\pi}\int_0^\infty \frac{\delta n'(x)}{x - \omega}\,dx \quad (45\text{–}46)$$

The total dichroic and birefringent contributions of intensity follow the relation:

$$\begin{aligned}\text{const.} \cdot I_b/I_o &\approx \int_0^\infty \delta n'^2(\omega)\,d\omega = \int_0^\infty \left[\delta n'(\omega)\frac{1}{\pi}\int_0^\infty \frac{\delta n''(x)}{x - \omega}\,dx\right] d\omega \\ &= \frac{1}{\pi}\int_0^\infty\int_0^\infty \frac{\delta n'\delta n''}{x - \omega}\,dx\,d\omega = -\int_0^\infty \left[\delta n''(\omega)\frac{1}{\pi}\int_0^\infty \frac{\delta n'(x)}{x - \omega}\,dx\right] d\omega \\ &= \int_0^\infty \delta n''^2(\omega)\,d\omega \approx \text{const.} \cdot I_d/I_o \end{aligned} \quad (47)$$

Thus, in combination with a continuum source and under conditions of the square-law characteristic at low atomic densities, the contributions from dichroism I_d and birefringence I_b are equal. With line sources, the respective relations between the dichroic and dispersive contribution are more complicated.[42]

At higher atomic densities, Equations 37 and 38 lose validity. The contribution of dichroism comes into saturation. Dispersive phase retardations can attain multiples of 2π and cause oscillations of the cosinus terms in Equations 35 and 36. However, with a broadband or continuum source and under the given Doppler-limited conditions ($\Delta \gg \Gamma$), the total intensity still increases with increasing density in a certain range of saturated dichroic contribution (see Section III.A).

III. BASIC EXPERIMENTS — FUNDAMENTAL RESULTS

A. Spectroscopic Properties of CFS

Figure 10 shows the calculated spectral transmission of a Voigt configuration with the D_1 line of a sodium vapor at low buffer gas pressure and at different atomic number densities n_A. At low atomic density, dichroism contributes Gaussian profiles, which are proportional to B_i^2 and centered to the Zeeman components of the line. The birefringent term, proportional to B_r^2 contributes additional intensity at the wings of the Zeeman lines.

The total intensity and its contributions, calculated as a function of the atomic number density by integration of the spectral profiles, are given in Figure 11. At low atomic and low optical density ("weak scattering limit"), it follows a square-law characteristic. If the source line is broad compared with the CFS line structure, especially if continuum sources are used, we find equal total contributions from dichroism and birefringence, since the areas under the birefringent and under the dichroic CFS profiles and thus both total contributions are equal (see Equation 47). However, at higher atomic densities ("multiple scattering limit"[1]), the two contributions behave differently. In the given example with Gaussian broadening, the dichroic intensity is saturated first, while the birefringent intensity for a certain range of atomic density still follows nearly a square-law characteristic. This rise of

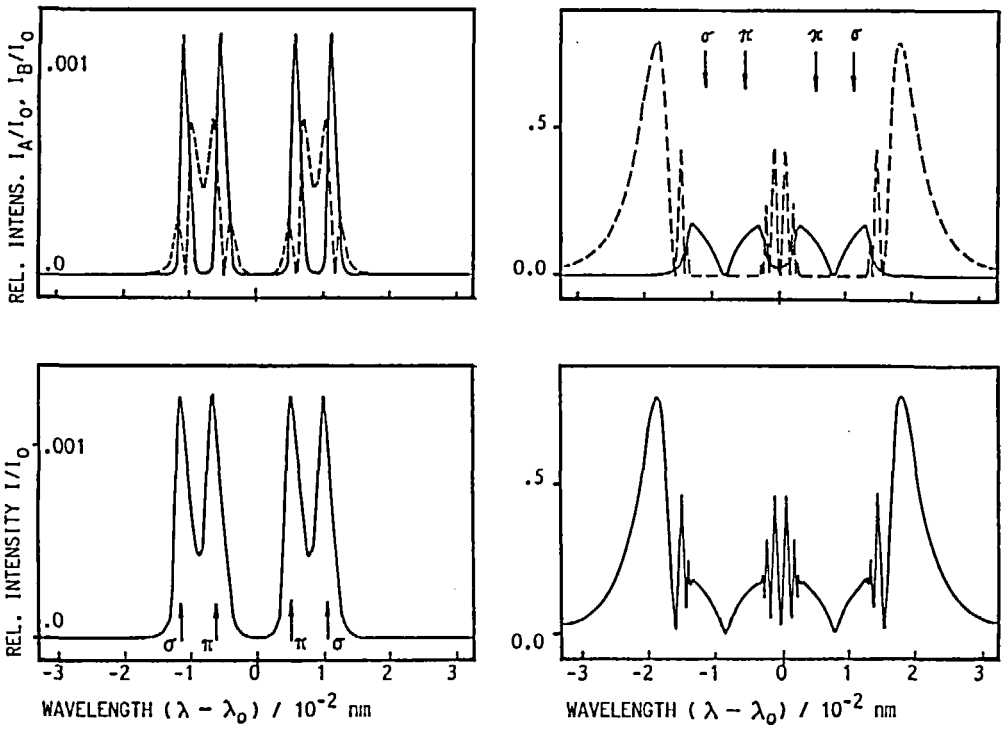

FIGURE 10. CFS line profiles calculated for the Na D1 line in a sodium vapor in a Voigt configuration at different atomic number densities and low pressure of buffer gas [100 Pa argon, upper row: dichroic intensity I_A (unbroken lines) and birefringent intensity I_V (dashed lines), lower row: total spectral transmission, left: $n_A = 5 \cdot 10^{10}$ cm^{-3}, right: $n_A = 10^{14}$ cm^{-3}].[29]

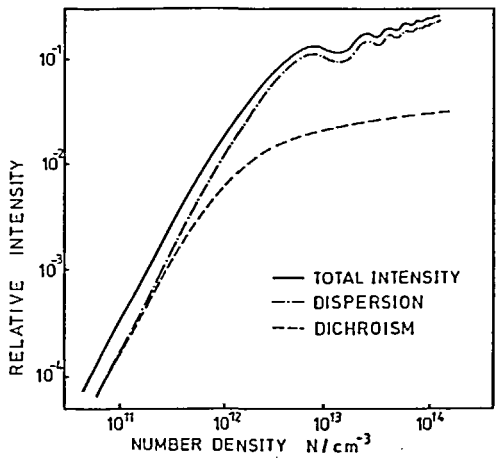

FIGURE 11. Total intensity transmitted by a CFS Voigt configuration and its contributions from dichroism and birefringence as a function of atomic density calculated by integration of the spectral profiles as shown in Figure 10 (B = 1 T).[43]

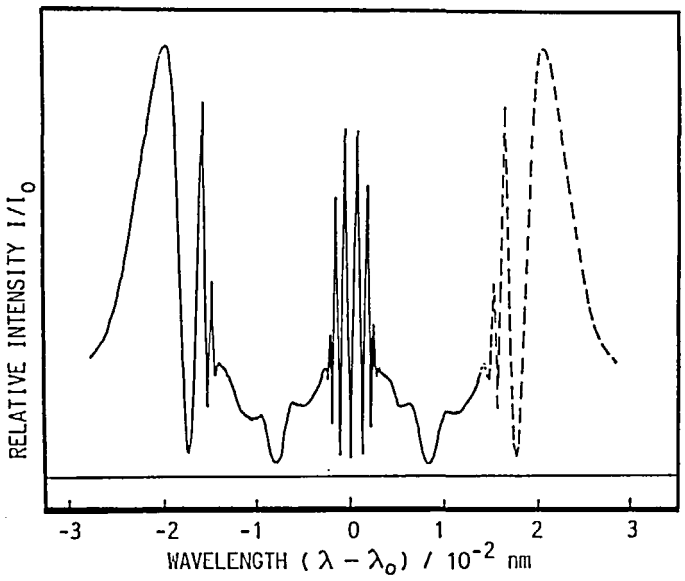

FIGURE 12. Measured Na D1 CFS line profile, recorded with a dye laser (line width 10^{-6} nm), scanning the line of sodium vapor in a Voigt configuration with a magnetic field strength of 0.5 T at 100 Pa argon buffer gas pressure.[29]

the total intensity results from the further increasing area under the broad birefringent contribution at the wings of the CFS line profiles, which then can extremely exceed the total dichroic intensity.

With the beginning of spectral oscillations, the slope of the total intensity is reduced but increases further with about $n_A^{1/3}$. However, calculations for Lorentzian-limited conditions show strong absorption from the broader imaginary part of the plasma dispersion functions, which partly covers the spectral range of the dispersive contributions on the line wings. Thus, in the Lorentzian limit at atmospheric pressure of buffer gas, the dichroic total intensity can exceed the birefringent contribution in a certain range of high atomic density.[43]

Figure 12 shows the measured profile of the CFS sodium D_1 line. It has been recorded with a cw dye laser by scanning the line. A cell has been used containing sodium [n_A(Na) = 10^{14} cm^{-3}] at low argon buffer gas pressure. In good agreement with the profiles calculated for high atomic density (Figure 10), it shows spectral oscillations which result from the dispersive birefringence with phase retardations of multiples of 2π and saturation of the dichroic intensity. The complete spectral profile of this CFS line is transmitted in combination with continuum spectrum sources.

CFS is an optical atomic resonance interaction technique with probing by light of an external source. Thus, CFS spectra are spectra of resonance lines only, without ion lines and without lines from higher excited states. CFS spectra include much less lines than atomic emission spectra and require much less resolving power of the spectrograph. By means of continuum spectrum sources, CFS resonance line spectra of an atomic vapor can be measured sequentially or simultaneously in a wide range of wavelengths (λ = 190 to 770 nm). Figure 13 presents the spectrum of a mixture of diluted standard solutions containing Cr, Fe, Ni, Mn, Na, K, Tl, Cu[44] in different concentrations. It has been recorded simultaneously by a photodiode array with a Voigt configuration and flame atomization. The intensity of each of the transmitted lines increases with increasing concentration following a square-law characteristic as expected from theory. Figure 14 shows the measured calibration characteristic for sodium under conditions as assumed for the calculated profiles presented in Figure 11.

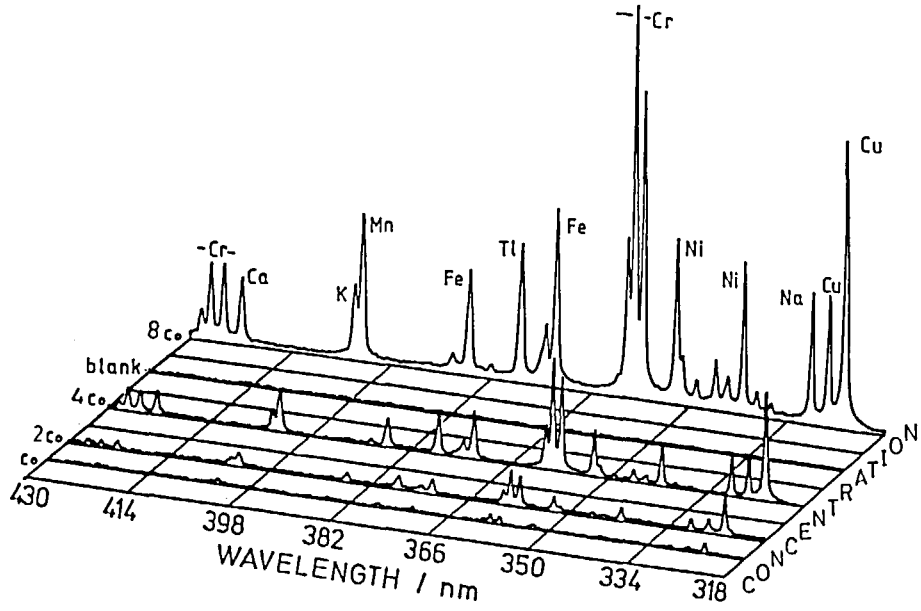

FIGURE 13. Spectrum of a mixture of diluted standard solutions containing (element [C_0/(μg/mℓ)]): Cr[25], Fe[12.5], Ni[6.25], Mn[2.5], Na[25], K[25], Tl[12.5], Cu[2.5], at different concentrations $c = k \cdot C_0$, recorded with flame atomization (not the strongest lines of the elements are detected).[44]

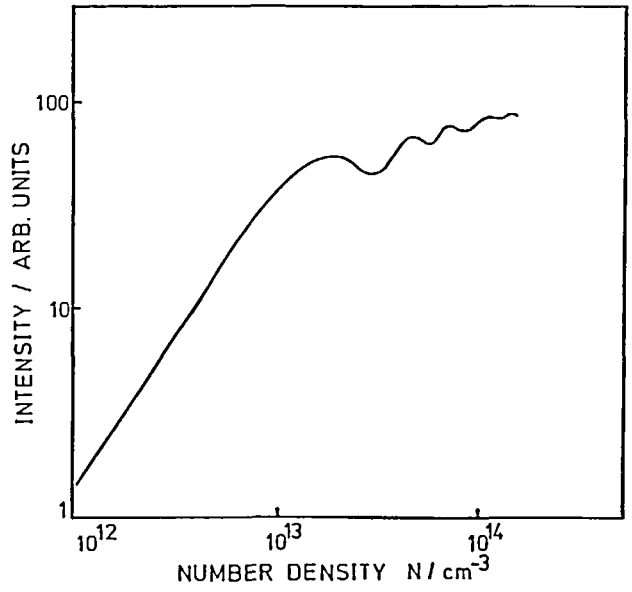

FIGURE 14. CFS calibration curves of the Na D1 line measured with a continuum source and a cell at low argon buffer gas pressure in a Voigt configuration (B = 1 T).[43]

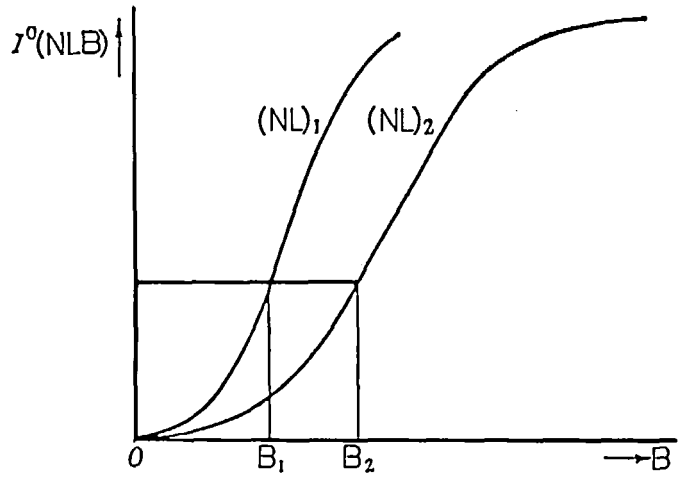

FIGURE 15. Schematic CFS zero-field line-crossing curve for different atomic densities.[1]

Using CFS with single-element line sources, as in AAS, only the element lines of the employed source can be detected. Church and Hadeishi[9] investigated line-crossing profiles of Hg 204 under low pressure conditions, in the limit of Gaussian line broadening, as well as under atmospheric buffer gas, with a Lorentzian broadened line-crossing profile, and published very early trace element detection based on CFS.[23,24,45] They determined mercury vapor in air, which had been injected into an argon carrier gas flow in a Faraday field configuration. In these early experiments, detection limits were confirmed in the range of 1 μg Hg/m³ air. Very interesting detection limits have been published for other elements too.[25,26,44,46,47]

However, the main advantage of CFS is the feasibility of real multielement determination in combination with continuum spectrum sources[25,26,28,29,34,48,49] as shown with the example of the simultaneously detected spectrum in Figure 13.

B. The Magnetic Line-Crossing Profile

Due to the higher spectral intensity and higher spectral resolution, CFS has been investigated first with atomic line sources. By use of the same isotopic composition in the source as in the interaction vapor, the line is centered mainly to maximum of the dispersive real part of the Faraday function $F_r(\omega - \omega_0, B_o)$ in a Faraday configuration or to the maximum of the dichroic imaginary contribution of the birefringence function $Bi(\omega - \omega_0, B_o)$ in a Voigt configuration, respectively. Corney et al.[1] discussed in their early paper the CFS intensity as a function of the applied magnetic field. Figure 15 shows the increasing CFS intensity with increasing magnetic field for different atomic densities. Its shape is likely the shape of a zero-field level-crossing signal ("Hanle curve"). Since, in low atomic density limit ("weak scattering approximation"), the width of the signal is given by the Doppler-broadened line width and not by the natural atomic line width, as that of the Hanle signal, the CFS intensity as a function of the magnetic field is called "line-crossing" curve (see also Sections I.A and IV.B).[1,5,9]

The behavior of the line-crossing curve as a function of weak magnetic fields can be derived by expansion of the Faraday function in Equation 39 or the birefringence function in Equation 40, respectively. In combination with a line source with its line centered to the atomic resonance line profile ($\omega = \omega_o$), it follows a square-law characteristic proportional to B_o^2 for the Faraday configuration (Equation 48) and a characteristic proportional to B_o^4

for the Voigt configuration (Equation 49). For Gaussian broadening ($\Delta \gg \Gamma$) we find (with $\Omega = g\mu B \cdot B/\hbar = g(e/2m)B_o = \gamma B_o$, γ gyromagnetic ratio):

$$I_F = I_o(3n_A e^2 f/[2\Delta \cdot \epsilon_o mc \cdot \Xi(JJ')])^2 (L/\lambda)^2 (\gamma/\Delta)^2 B_0^2 \quad (48)$$

$$I_v = (\pi/16)\, I_o(3n_A e^2 f/[2\Delta \cdot \epsilon_o mc \cdot \Xi(JJ')])^2 (L/\lambda)^2 (\gamma/\Delta)^4 B_0^4 \quad (49)$$

At low atomic density (weak scattering limit), the line-crossing profile is given by the profile of the Faraday function $|F(\omega - \omega_o, B_o)|^2$ or the birefringence function $|B(\omega - \omega_o, B_o)|^2$ of the magnetic field B_o. At high atomic density n_A, Equations 37 and 38 and the expansion of the cosinus in Equations 35 and 36 are no longer valid, and Equations 50 and 51 describe the spectral CFS profiles:

$$\begin{aligned} I_F &= (I_o/2)|\sin(\pi \cdot \Delta n_F \cdot L/\lambda)|^2 \exp(-4\pi n_F'' L/\lambda) \\ &= (I_o/4)\,\{1 - \cos[\text{const.} \cdot n_A(L/\lambda)(\gamma/\Delta)B_o]\}\exp(-4\pi n_F'' L/\lambda) \end{aligned} \quad (50)$$

$$\begin{aligned} I_v &= (I_o/2)|\sin(\pi \cdot \Delta n_v \cdot L/\lambda)|^2 \exp(-4\pi n_v'' L/\lambda) \\ &= (I_o/4)\,\{\cosh[\text{const.} \cdot n_A(L/\lambda)(\gamma/\Delta)^2 B_0^2] - 1\}\exp(-4\pi n_v'' L/\lambda) \end{aligned} \quad (51)$$

Equations 50 and 51 represent the zero-field line-crossing profiles for measurements with line sources in the range of weak magnetic field strengths. At high atomic density, the interference term $|\sin(\pi\Delta nL/\lambda)|^2$ is passing its maximum before the maximum of the Faraday function $|F(\omega - \omega_o, B_o)|$ or the birefringence function $|F(\omega - \omega_o, B_o)|$, respectively, is attained. Thus, the width of the line-crossing signal is getting much narrower than the magnetic Faraday profile or the magnetic Voigt profile. This effect is described as "coherence narrowing" in the "multiple scattering" limit,[1] which is shown in Figure 15 for different atomic number densities.

Due to the real part of the argument of the cosinus in Equation 50, oscillations of the line-crossing signal occur by using a line source in a Faraday configuration as shown in Figure 16. Smoothing of these oscillations with increasing field depends on the spectral width of the source line. And, especially in Faraday configurations, with increasing magnetic field the overlapping of the resonance line with the source line decreases due to increasing Zeeman splitting. Thus, the absolute value of the Faraday function $|F(\omega = \omega_o, B_o)|$ decreases again at high magnetic fields.

Figure 17a presents the complete zero-field line-crossing curve of a Hg 198 vapor in a Faraday configuration with a line source containing pure Hg 198 measured by Hackett and Series.[5] Figure 17b shows again the line-crossing curve under the same conditions as Figure 17a, but with the vapor cell containing mercury with natural isotopic abundances. The intensity increases with the magnetic field increasing from zero ("zero-field line-crossing"). However, there are further minima of the transmitted intensity at 0.11 and 0.24 T. Figure 18 shows the magnetic line splitting pattern and the line-crossing profile of a Hg 200-Hg 202 isotope mixture, measured by Siegmund and Scharmann[8] with the sharp high-field line-crossings, appearing when different counterpolarized components of the related isotopes are simultaneously in resonance.

The curves in Figure 19 represent zero-field line-crossing signals, measured with silver in a Voigt configuration, but atomized by a flame under atmospheric pressure and with different widths of the source lines. It shows that the line-crossing signal is broadened with increasing width of the source line and that its high field maximum is getting flatter. Using

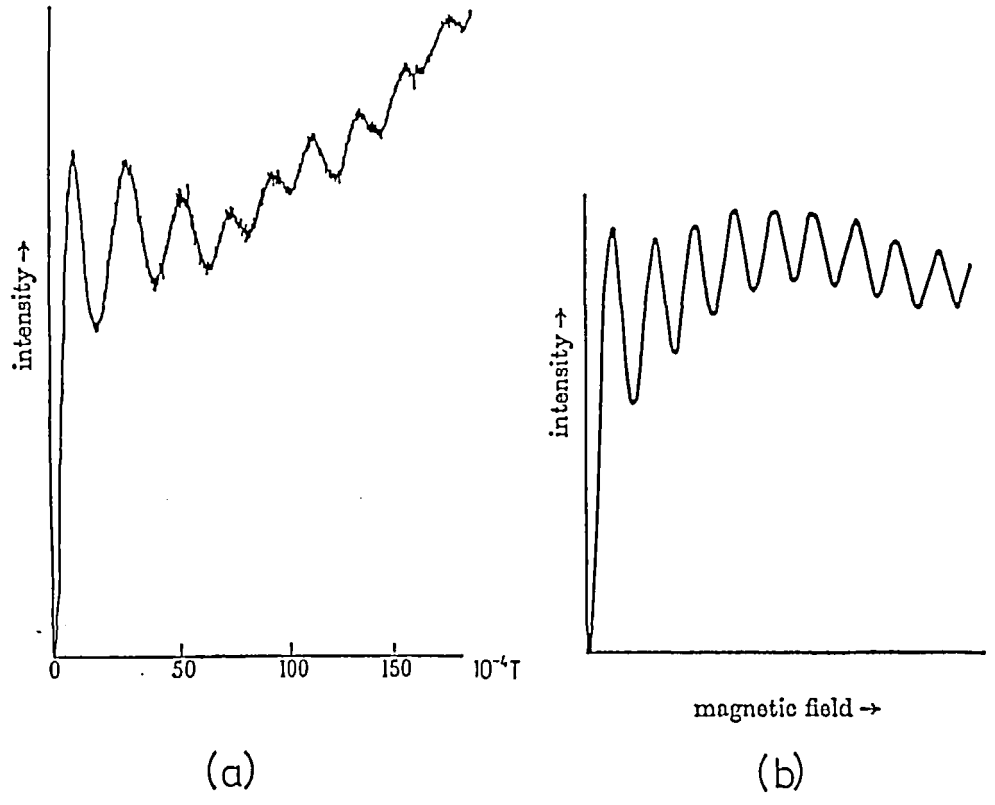

FIGURE 16. Measured (a) and calculated (b) zero-field line-crossing signal with strong coherence narrowing and oscillations due to large phase retardations in a Faraday configuration with source and cell containing Hg vapor (Doppler limited).[1]

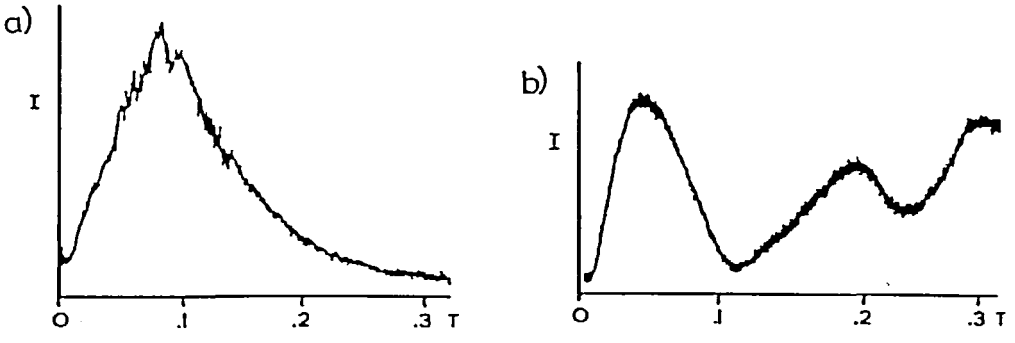

FIGURE 17. CFS intensity of a Faraday configuration as a function of magnetic field (line crossing). Source: air-cooled microwave lamp containing Hg 198, vapor cell at 0°C containing: (a) Hg 198 and (b) natural isotopic abundance of Hg (Hg 198: 10%, Hg 200: 23%, Hg 202: 33%).[5]

continuum sources, this maximum is attained beyond the strength of 1 T and very flat, more like a saturation profile. Especially in Voigt configurations there is no sharp maximum of the CFS intensity as a function of the applied magnetic field.[35] In principle, this maximum is passed at lower field strengths in a Faraday configuration than in a Voigt configuration. A detailed discussion of field optimization is given in Section VI.A.

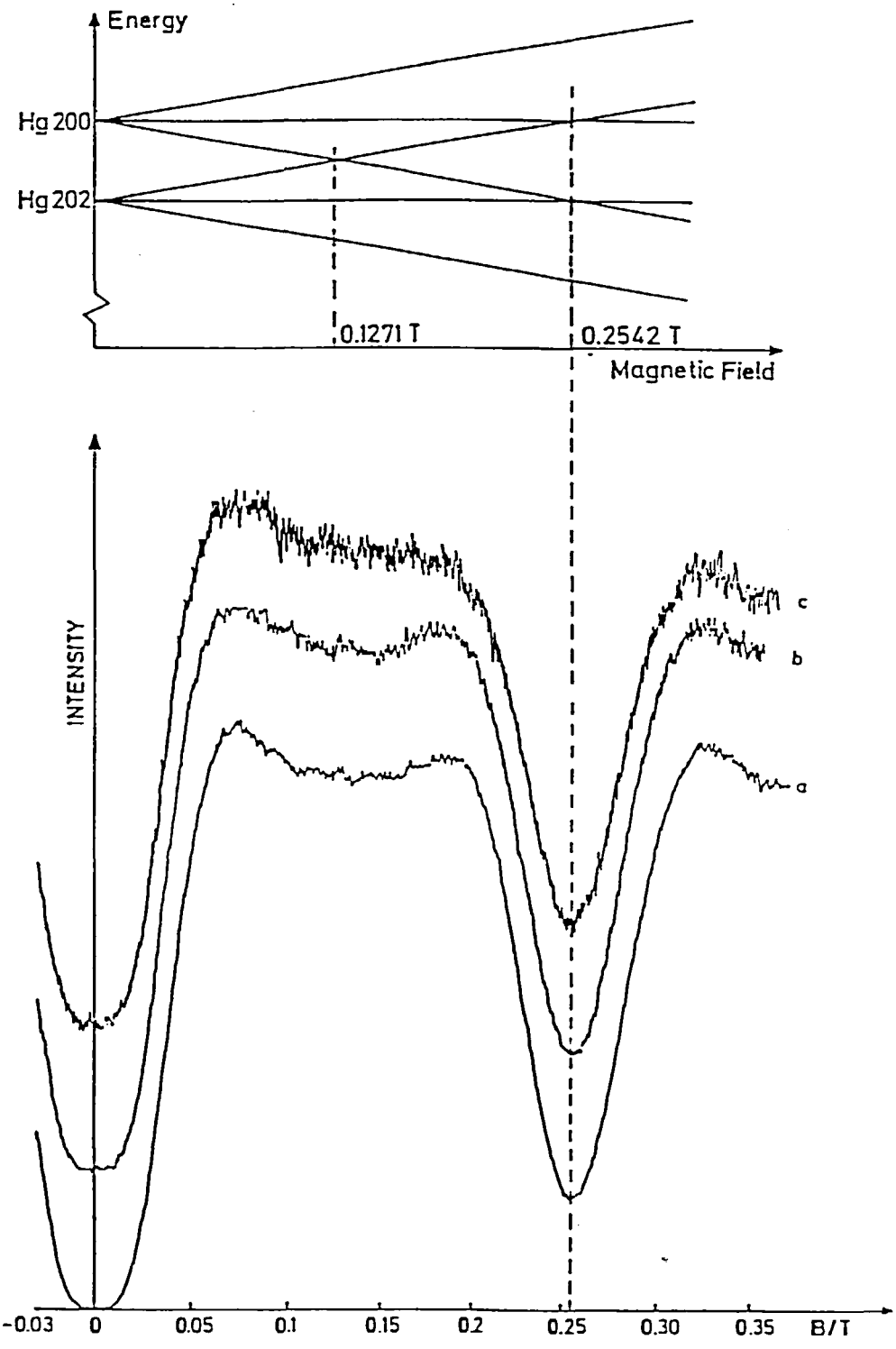

FIGURE 18. Zeeman-splitting pattern of the lines of the isotopes Hg 200 and Hg 202 as a function of the magnetic field and the line-crossing profiles measured in a Voigt configuration.[11]

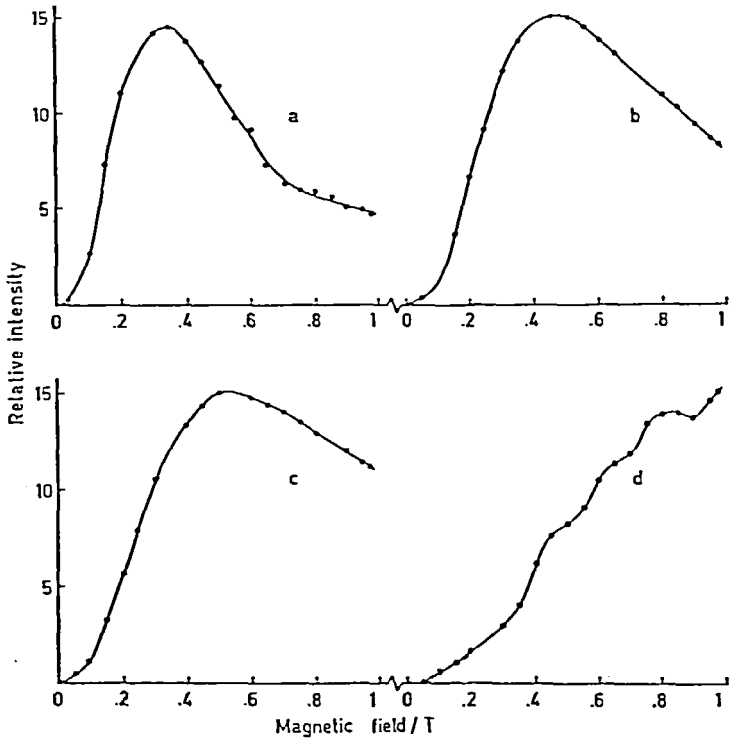

FIGURE 19. Transmitted intensity of a Voigt configuration; flame atomization by injection of a 25 ppm Ag solution.[66] Sources: (a) hollow-cathode lamp, d.c. mode (4 mA); (b) pulsed mode (330 Hz, 500 μsec, 30 mA); (c) pulsed mode (330 Hz, 15 μsec, 250 mA); (d) deuterium lamp (15 W d.c.).

IV. SPECIAL ANALYTICAL PROPERTIES OF CFS

A. The Feature of a Zero Method

In combination with a crossed polarizer-analyzer pair, CFS is a zero method. This means that, under ideal conditions, the CFS intensity is zero for zero atomic density in the analyte vapor. The signal is generated — like in OES — directly by optical means without modulation and lock-in detection. Nevertheless, CFS is — like the AAS — an approach of atomic resonance interaction spectroscopy with probing by light from an external source. Thus, CFS produces much less lines than obtained in emission spectra and therefore requires much less spectral resolving power. Figure 20 illustrates the principle properties of signal generation by time-sharing modulation and lock-in technique and of direct signal generation as via CFS. It also shows the characteristic contributions of noise for both approaches.

If the signal is generated directly by CFS, the flicker noise of the source is reduced to the fraction related to the transmitted signal intensity and its main contribution is blocked together with the basic intensity. By the same reason, background due to unspecific absorption is reduced to its signal fraction too.

In contrast to ZAAS, where background absorption and source noise enter with the full total detected intensity, I_o, all noise contributes twice: via signal detection and via background detection. At the characteristic absorption, both contributions are of the same order of magnitude. And, in consequence of modulation, the detection time for both signal and background is reduced to less than half of the total time of the measurement.

Since the CFS signal can be recorded in principle without need of modulation and lock-

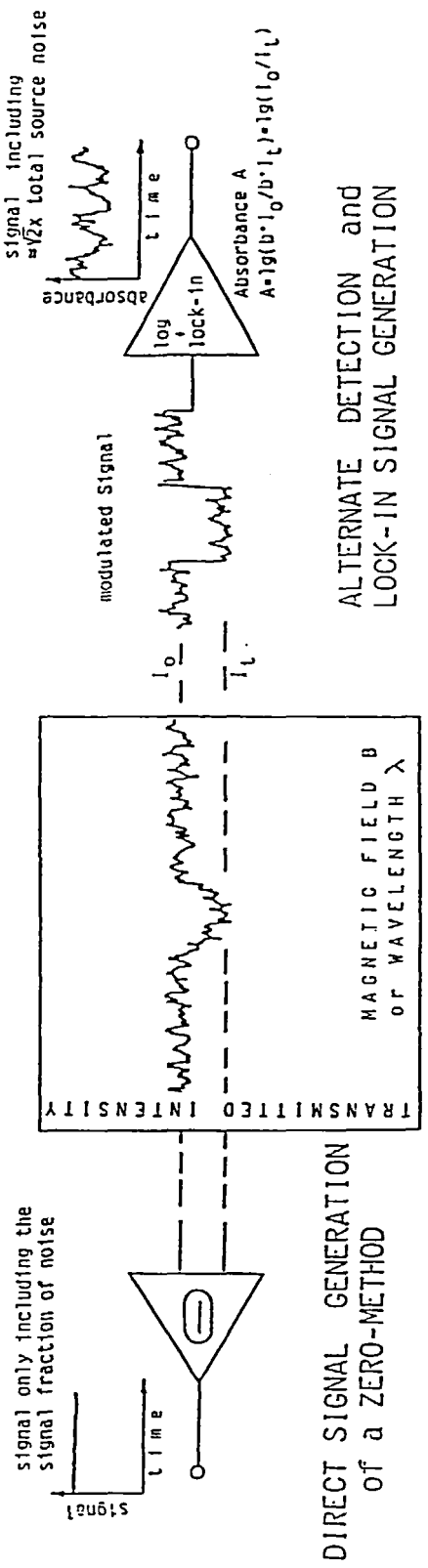

FIGURE 20. Principle of signal generation directly with a zero method and by lock-in detection.[91]

in detection, modulation techniques can be optionally provided for detection and correction of background. Modulation of CFS parameters enables the user to detect and correct background due to unspecific intensity as from incomplete polarizer extinction, emission or foreign light from the furnace, as well as from background due to unspecific absorption. A more detailed discussion of approaches of separate detection and correction of noise and background is given in Section VII.

By using a continuum spectrum source, first the off-resonant intensity is suppressed mainly by the zero-method feature, and second the background intensity is mostly unstructured. As known from the OES, by using a zero method and in absence of structured background, background intensity can be determined from the baseline of the spectrum. Reduction of the intensity by a zero method allows the application of more sensitive detectors and improvement of the dynamic range. This dynamic range is limited mainly by the wide dynamic range of optical detectors and by noise.

These inherent properties include suppression of the source noise and interferences due to unspecific absorption to the signal fractions of each of these quantities. Furthermore, as shown below, the advantage of a zero method includes optimum conditions for real time-resolved detection, which helps to find out matrix interferences in combination with ETA.

B. The Square-Law Characteristic

Under conditions of a crossed polarizer-analyzer configuration, the CFS intensity follows a square-law characteristic. Square-law response is a property of interference spectroscopy and polarization spectroscopy under conditions of complete extinction of the primary probe light. On the other hand, this feature characterizes any intensity that results from coherent contributions of an ensemble in general. A detailed discussion of the effect of coherence in connection with CFS has been published by Durrant.[50] By means of the autocorrelation function, the macroscopic and the discrete nature of the atomic vapor are described, and it is shown that the total transmitted CFS intensity from a broadband source is given by two contributions. Equation 52 gives a reduction of the result:

$$I_{CFS}(\omega, \Phi) = C'I_o\{(1/\Delta)|N \cdot S(\Phi) \sum a_q Z_q|^2 + (1/\Gamma)N \sum |a_q L_q|^2\} \quad (52)$$

where N represents the total number of resonant atoms in the active vapor; C′ is an expression of relevant constants; and S (Φ) considers the diffraction due to the finite extension of the vapor cell (Φ = angle of observation). The functions $\Sigma a_q Z_q$ and $\Sigma|a_q L_q|^2$ are expressions of counterpolarized components $Z_q(\omega - \omega_o)$ of the plasma dispersion function and the complex Lorentzian:

$$L_q(\omega - \omega_o, \Gamma) = 1/[\omega - \omega_o - \{g_e m_e - g_i(m_e + q)\}\Omega + i\Gamma] \quad (53)$$

respectively. According to the Faraday function or the birefringence function [$F(\omega - \omega_o, B_o)$, $B(\omega - \omega_o, B_o) = \Sigma a_q Z_q$], the constants a_q, as given with Equation 32, depend on the geometrical field configuration.

If the source intensity is switched off at t = 0, damping of coherent and incoherent contributions of Equation 52 appears quite different. Damping of the Lorentzian contribution (second term), which represents incoherent atomic resonance fluorescence and level-crossing phenomena, is described by the time constant $\tau = 1/\Gamma$, with a corresponding exponential decay proportional to $\exp(-\Gamma t)$. However, damping of the macroscopic coherent contribution is mainly given by dephasing of the ensemble due to the atomic velocity with the time constant $\tau = 1/\Delta$, and the corresponding Gaussian decay is described by $\exp(-\Delta^2 t^2 - \Gamma t)$. This first term of Equation 52, related to coherence of an ensemble of different atoms, represents the CFS and the line-crossing[5] phenomena (see Sections I.A and III.B).

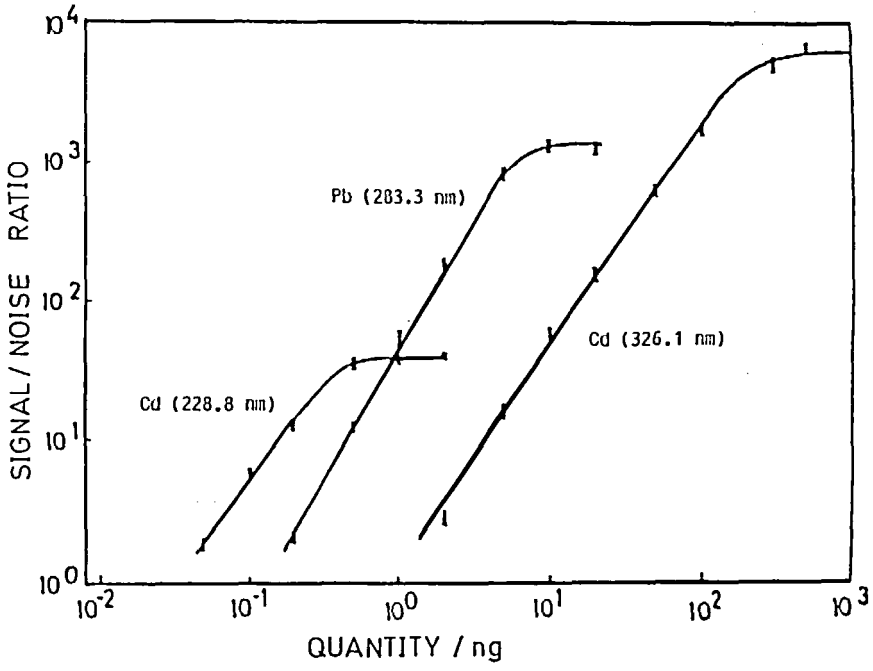

FIGURE 21. Graphite furnace calibration characteristic measured sequentially by a photomultiplier.[77]

As shown in the cited work,[50] the macroscopic coherent CFS intensity exceeds the incoherent fluorescence with a factor $NS^2(\Phi)\Gamma/\Delta$, i.e., under experimental conditions by many orders of magnitude. Compared with incoherent fluorescence, the CFS intensity is strongly enhanced by coherence. In forward direction, coherent CFS is so intensive that incoherent fluorescence is completely covered. Furthermore, the square-law characteristic of CFS, which can be regarded as a result of coherence, causes dynamic signal expansion. Small relative changes of analyte vapor densities result twice in related changes of the transmitted intensity. This expansion of the analytical signal means improved analytical resolution by improved relative sensitivity $(dI/I)/(dn_A) \approx 2$, which is equivalent to the logarithmic slope.

All optical interferences, background due to unspecific absorption as well as unspecific emission, influence the detected intensity. Thus, dynamic expansion of the CFS intensity means, on the other hand, dynamic compression of the analytical effect of background, which is detected with the spectral line intensities. With the analytical calibration of CFS, which mainly follows a square root, the effect of noise and background of the whole optical channel is reduced to half of the detected relative amount:

$$dI/I = 2\, dn_A/n_A \qquad dn_A/n_A = (1/2)\, dI/I \tag{54}$$

In general, the measured calibration characteristics may differ slightly from the square-law characteristic. Figure 21 (see also Figure 28) shows, inter alia, as a quite extreme example, the calibration function for Cd measured with GF-ETA on the strong 228-nm resonance line. The detection range of this characteristic is not far from saturation at a total analyte mass of about 100 pg.[25] In the given range, the slope is that of a characteristic proportional to $n_A^{1.4}$. In principle, linearization of the analytical response is ensured by calibration by measurement of the calibration characteristic, logarithmic interpolation, or interpolation on the basis of the power law which is fitting the calibration measurements. If the apparatus is operated computer-controlled, linearized spectra may be recorded by

storing the roots of the detected intensities. Approaches of direct optical linearization are presented in Section VI.B. By means of linearized time-resolved spectra, optimal ETA peak-area data are obtained.

In principle, the increased relative sensitivity due to the square-law effect has to be payed by a reduction of dynamic range. The intensity decreases with high slope with decreasing vapor density. Thus, the detection limit at a twice rms noise signal is attained at much lower intensity. However, since the dynamic range of photodetectors is generally high, and since the basic intensity and its noise limit are very low, good polarizers assumed, the loss of dynamic range due to the square-law properties is considerably compensated by the dynamic effect of a zero method. Furthermore, CFS will be provided for simultaneous or sequential multielement determination, and a complete spectrum of lines of different strengths may be recorded in one measurement. Thus, the range of detected concentrations can be extremely extended, especially into the range of high concentrations.

C. Atomic Zeeman Spectra

As well known from ZAAS in direct or inverse technique,[21,22] properties of CFS depend on the Zeeman structure of the employed line, which is related to the quantum numbers of the atomic levels, and g factors. The real line structure furthermore depends on the isotopic and hyperfine structure of the measured resonance line.

The resonance spectra of the group IIa elements of the periodic system are mainly pure singulet spectra and show the normal Zeeman effect. The same is valid for the far stronger lines of the lighter group IIb elements Zn (219.8 nm) and Cd (228.8 nm). In addition, the total angular momentum J of the ground state of these elements is zero, as of the elements of group IVb, including the heavy metals Sn and Pb. Thus, despite hyperfine structures of odd isotopes, the resonance lines of these elements split into simple Lorentzian triplets. Under these conditions of a pure Lorentzian triplet, the CFS line profile results with the same shape for all magnetic sublevels m_g in Equation 28 with functions $B(\omega,B_o)$ or $F(\omega,B_o)$ as shown in Figure 9 without additional structure, or broadening due to anomalous Zeeman effect.

If both ground state and excited state split up differently ($J_e,J_g > 0$ with different Landé-factors g_e, g_g), then the Zeeman structure depends on both angular momentum and Landé factors. Typical splitting patterns of elements with an odd (J_e, J_g = half-integer) or even (J_e, J_g = integer) number of valence electrons and with an even or odd number of Zeeman lines (with the correct sign of contribution to the birefringence function for the Voigt configuration) are shown in Figure 22. Convolution of these patterns with the real and imaginary parts of the plasma dispersion function results in the real and imaginary parts of the birefringence function. Thus, the spectral profiles of dispersion as well as dichroism are broadened and smoothened by the envelopes of the Zeeman patterns.

In general, a convolution of the plasma dispersion function has to be carried out with the isotopic Zeeman line structure, including hyperfine splitting and isotope shift. A detailed discussion of isotopic effects in combination with CFS on the basis of different analytical examples is given by Kitagawa et al.[51,52] Figure 23 presents the line-crossing profile of the 324.8 nm D_2 line of copper, which is related to the $4^2S_{1/2} -> 4^2P_{3/2}$ CuI transition, measured in a Faraday configuration. The hyperfine Zeeman splitting pattern of the corresponding transition is shown in Figure 24. Copper has the isotopes Cu 63 and Cu 65 both with nuclear spin I = 3/2. The minimum at B = 0 T is the zero-field line-crossing minimum; the second minimum is related to the "hyperfine high-field line-crossing" of the σ^+ and σ^- Zeeman lines in a magnetic field region of 0.3 to 0.45 T. The rapid decrease with increasing field beyond the strength of about 0.8 T is caused by the reduction of atomic resonance interaction with the narrow line of the hollow-cathode line source. In combination with broadband sources, the maximum of this curve will be very flat.

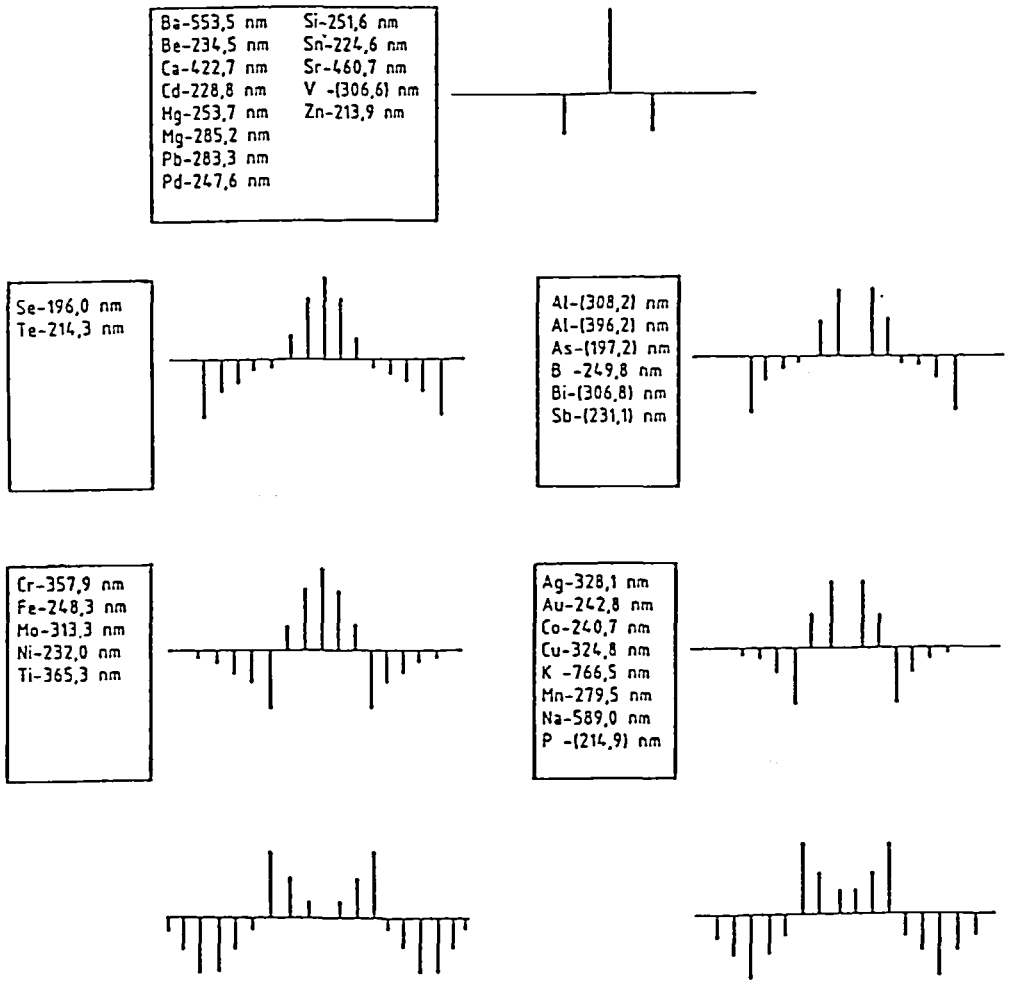

FIGURE 22. Different types of Zeeman structures with signs as they contribute to the birefringence function.[53] Top: normal Zeeman effect; second row: higher g_J related to state of higher J; third row: higher g_J related to lower J; bottom: equal J = J'; left: even; right: odd number of electrons.

In general, a complex magnetic splitting pattern causes reduction of the effective CFS line strength due to smoothing and broadening of the resulting birefringence or Faraday function in combination with the square-law response. Furthermore, the magnetic line-crossing profile becomes structured if isotopic high-field line-crossings or hyperfine level crossings occur.

V. EQUIPMENT, ANALYTICAL APPROACHES, AND APPLICATIONS

A. The Atomization Unit

CFS is an approach of atomic resonance interaction spectroscopy with external probe light, like the AAS. Thus, in general, all atomization systems, which are well known from atomic absorption spectroscopy,[53] can be used. The atomizer has to be placed in an external magnetic field, as for the inverse Zeeman technique. Constructions and alignments of flames and furnace units are simpler in combination with Voigt configurations than with Faraday configurations. Thus, despite slight advantages of the Faraday configuration with respect to detection limits and the optimal strength of the magnetic field, the Voigt configuration is preferred.

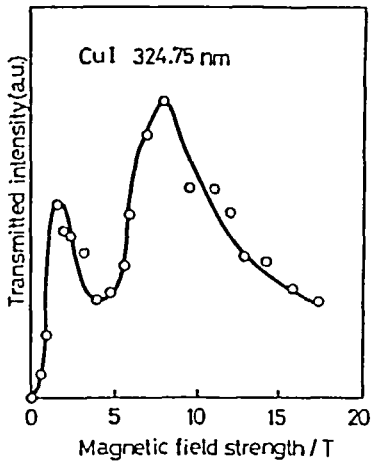

FIGURE 23. Line-crossing profile of the 324.8-nm D_2 line of copper, ($4^2S_{1/2} \rightarrow 4^2P_{1/2}$ CuI transition), measured in a Faraday configuration. The minimum at B = 0 T is the zero-field line crossing; the second "line crossing" is due to the "hyperfine level crossing" (also called "Doppler-broadened level crossing") of the σ^+ and σ^- Zeeman lines of the isotopes Cu 63 and Cu 65.[51]

Mainly ETA is applied, and mostly in GF-ETA[54,55] under atmospheric argon sheath gas. Thus, the whole atomization process[56-58] as well as interferences[59] and the conditions of temperature and vapor diffusion are well known from investigations with respect to the AAS. However, due to the square-law characteristic of CFS, the requirement of a high thermal furnace ramp rate is of even greater importance than in combination with the AAS. Approaches with pulsed heating[60] have to be considered with great interest. Boats or platforms,[61] and tube-in-tube techniques,[62] ensuring approximately thermal equilibrium with the tube atmosphere, are also very helpful tools. Takada and Hirokawa[63] demonstrated the advantages of a lidded cup cuvette for determination of Cd and Zn in high purity tin.

Improved atomizers combined with external magnets are commercially available for the inverse technique of ZAAS. The magnetic field strength and the constructions of such furnaces are well suited to be employed in an CFS apparatus. Thus, a CFS apparatus is very likely in a ZAAS spectrometer with inverse Zeeman technique. Figure 25 shows an apparatus for simultaneous multielement determination based on a commercially manufactured furnace and magnet unit with an automized analyte sampler (furnace unit HGA-600 with autosampler AS60, Bodenseewerk Perkin-Elmer and Co.GmbH, Überlingen, West Germany). The detector is a photodiode array with a channel plate as an optical preamplifier. The continuum source is a 1000-W Xe lamp. A furnace unit with a permanent magnet also has been used very successfully in combination with CFS.[63]

Compared with ETA, flame atomization is characterized by higher precision of vaporization and better reproducibility of the measurements. On the other hand, the detection limits are two or three orders of magnitude higher than those for ETA.[64] Constructions of favorable flames, in the common form of laminar burners with a long-slit nozzle, are even more restricted to Voigt configurations than are furnaces.

B. Light Sources, Optics, and Detectors

Hollow-cathode lamps are predominantly employed as line sources. In addition, high-frequency and microwave-coupled sources, which can produce higher intensities, and a.c.

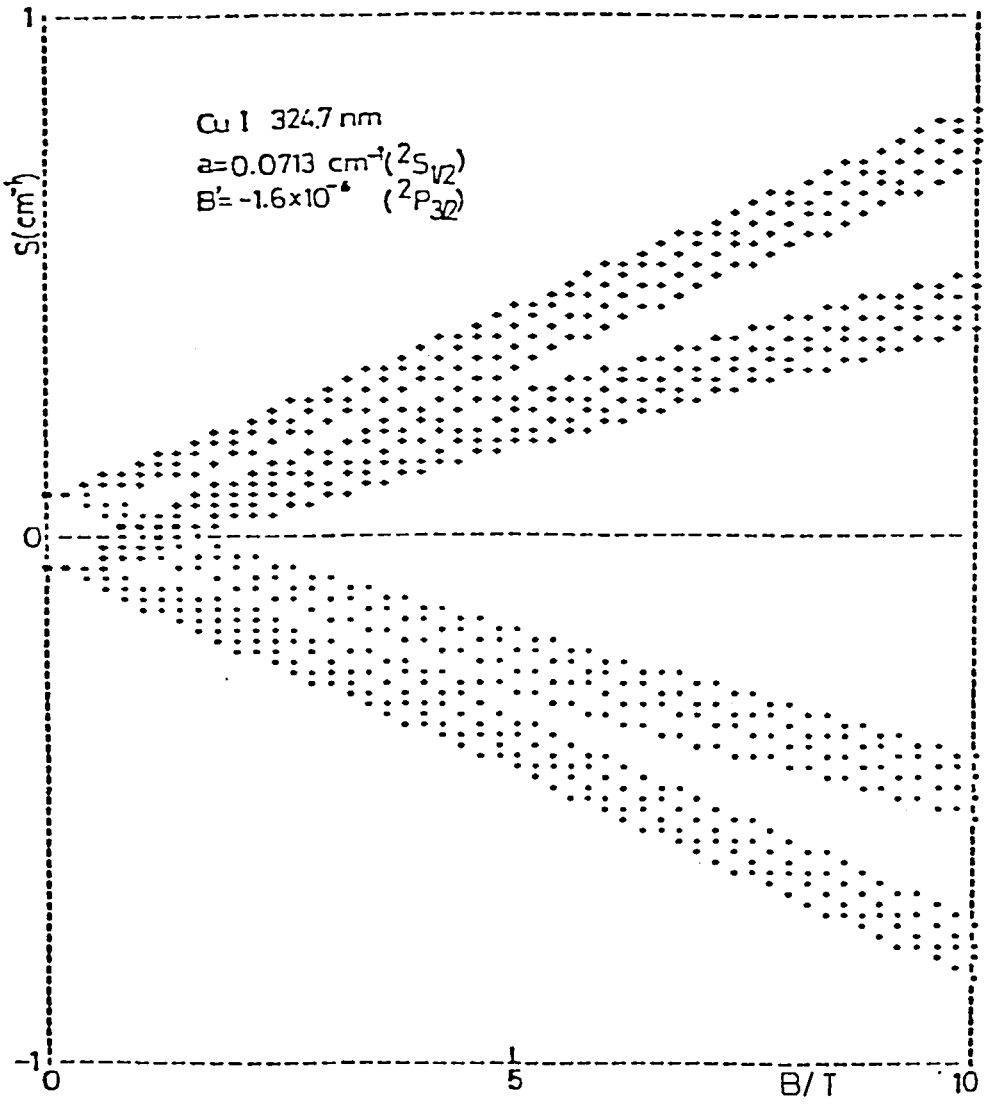

FIGURE 24. Hyperfine line-splitting pattern (Cu with the isotopes Cu 63 and Cu 65 both with nuclear spin I = 3/2) as a function of the magnetic field (they assume a higher hyperfine splitting constant of ground state).[51]

as well as d.c. supplied low pressure discharge lamps are used. Line profiles of sources can be broadened by pulsed operation at a higher discharge current.[65] The radiant densities of efficient element line sources exceed the radiant densities of intensive continuum sources and the fraction of intensities which are related to the spectral width of the CFS line by a factor 10^2 to 10^4.

Therefore, due to the higher spectral radiant intensity, line sources commonly yield better detection limits than do continuum sources. However, disadvantage of continuum sources is partly compensated for by the spectral smoothness which allows optimal correction of background intensity. For elements with weak hollow-cathode line sources only (e.g., Ti), the detection limits of CFS by using a continuum source including the multielement capability can be even better than those of the single-element AAS with line sources, as shown by Ito.[26]

Employed continuum spectrum sources are predominantly Xe lamps ("short-arc" types

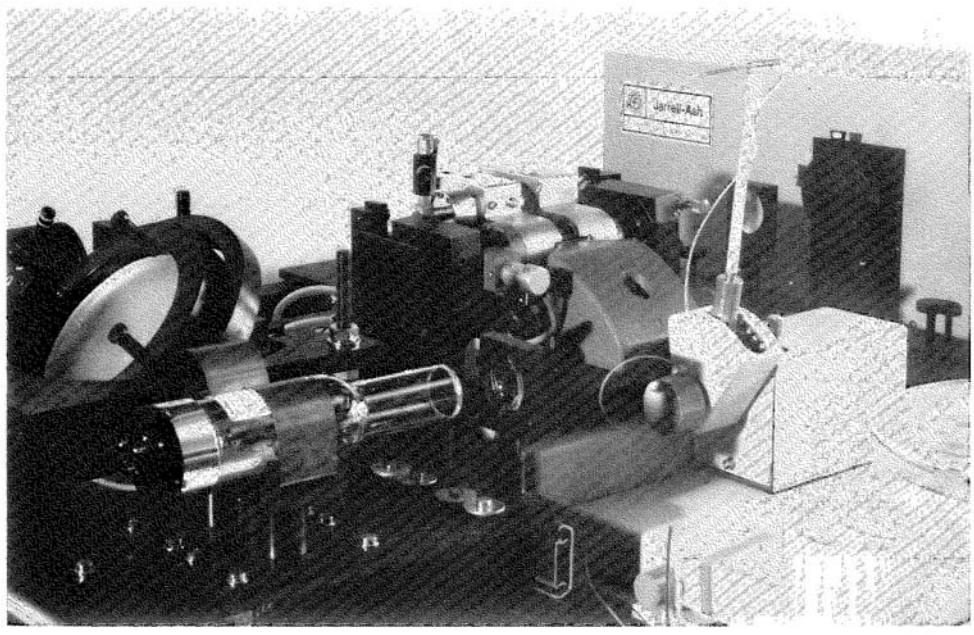

FIGURE 25. Apparatus for simultaneous multielement determination based on a commercially manufactured furnace unit with autosampler (HGA-5000, Bodenseewerk Perkin-Elmer and Company GmbH, Überlingen, West Germany), with (Osram XB01000W/4) continuum source and additional deuterium (200 W W.C. Heraeus Quarzlampen) and hollow-cathode lamps, a grating-polychromator with 25 cm focal length (Jarell Ash 82-499), and a photodiode array with a channel-plate optical preamplifier as detector.[64]

as Osram XBO, 75 to 1000 W). Very interesting lamps (totally sealed ceramic constructions including an integrated parabolic mirror) have been produced recently under the type declaration "Cermax" (ICL Technology or Oriel, Inc.) with a power range of 75 to 1000 W. Furthermore, deuterium lamps typically of 50 to 200 W are employed. A prototype of a 1000-W deuterium source has been tested successfully by Wirz, Debus, Hanle, and Scharmann.[34] Deuterium lamps have higher spectral intensities at wavelengths shorter than 225 to 260 nm, depending on the types. At longer wavelengths, Xe-arc sources are to be preferred. Thus, Xe lamps cover about the same spectroscopic range as Glan-Taylor prisms.

Each element line source must be considered individually. In particular, the operation may be attended by variations of line intensities, line profiles, and even line inversion. The individual conditions of vaporization or sputtering of the source element are not independent of the excitation conditions. However, linebroadening is favorable in combination with CFS[66] (see also Section V.C.1), and even line inversion has much less effect than in AAS since dichroism and birefringence of the Zeeman line together cover a wide spectral range.[67] Lifetimes of hollow-cathode lamps are very different. On the other hand, Xe-arc sources are characterized by great reliability, high stability, and long lifetimes, typically 2000 hr. In addition, continuum sources are almost free from rough spectral changes.

The properties of the polarizers, which have to block the basic probe light, are of crucial importance. For wavelengths longer than about 215 nm, air-spaced calcite prisms of the Glan-Taylor type, polarizing with their transmission in the extraordinary ray, are optimal. Such Glan-Taylor prisms are available, specified with an open transmission t_1 of up to more than 70%, with an extinction ratio of typically $t_2/t_1 = 10^{-5}$, and with up to 10^{-7} available for selected specimens. The angular aperture is of the same order of magnitude as that of common furnaces. However, the optimal angular orientation of Glan-Taylor prisms varies

slightly with the wavelength. Thus prisms, being manufactured for wavelengths of 400 nm, can be used in the whole analytical spectral range from the UV limit of calcite transmission up to the red. However, they have to be declined a few degrees against the optical axes to ensure optimal angular aperture.

In the shorter UV range — the limit will be the 213.8-nm line of Zn — the transmission of the extraordinary ray of calcite is decreasing very rapidly with decreasing wavelength. Polarizers in this shorter UV region are prisms of the Wollastone or Rochon type, made from quartz or magnesium fluoride. These prisms transmit both polarizations with an angular separation of about 1°. Thus, the useful angle of aperture is reduced beyond this angular separation of polarizations, and forward-directed scattering, especially Mie scattering due to smoke, dust, and scratches on optical surfaces, causes reduction of the effective extinction ratio. On the other hand, the detection of both polarizations allows various special approaches for background detection and correction (see also Section VII.B).[27,36,52,68,69]

In principle, polarization by sets of Brewster-angled plates can be considered as well. Since the extinction of calcite in the shorter UV region is much higher in the ordinary ray than in the extraordinary ray, polarization by dichroic absorption in calcite plates also can be taken into account.

Since CFS is a resonance interaction method, bringing only resonance lines of elements to transmission, the required resolving power of the monochromator is quite low. Small instruments with 10 to 50 cm focal length are sufficient. Typically, 25-cm grating spectrographs of the Czerny-Turner type (like Jarrell Ash 82-410) are used. The apparatus presented in Section V.C.3 by Figure 30 is operated with a very small instrument of 12.5 cm focal length (Oriel 7240). A very interesting approach is presented by Hirokawa and Namiki[70] by using an acoustooptic filter, which could be tuned by a sweep oscillator.

Detectors are mainly photomultipliers. Especially for detection of weak lines in combination with continuum sources, operation in cooled housings increases the signal-to-noise ratio. Weak line intensities can be measured with techniques of single-photon counting. Since resolving power, required for atomic resonance spectra, is considerably low, simultaneous multielement determination can be carried out by means of position resolving detectors as shown first by Wirz, Debus, Hanle and Scharmann[34] with a vidicon. Photodiode arrays[29,71] in combination with optical image amplifiers as proximity-focused amplifiers or predominantly channel plates are available with an efficiency and sensitivity comparable to the respective data of photomultipliers.

C. Analytical Approaches and Applications

1. Single- and Multielement CFS with Line Sources

The very early presentation of CFS as a tool for trace element determination has been given by Hadeishi et al.[23-24] with the example of mercury. Hanle, Scharmann, and Wirz[72] measured mercury in a sealed quartz cell. The determination of the heavy metal Cd by CFS has been studied very early as well.[25,46] Ito et al.[25] used an intensive electrodeless high-frequency discharge lamp in combination with an electrically heated furnace with a tantalum tube. A magnetic field of 1 T has been applied in Voigt configuration with a very advantageous single-Rochon double-path alignment, reflecting the light after polarization and one furnace transmission a second time through the furnace and through the same prism, acting simultaneously as the analyzer. Thus, one polarizer is spared and the optical path through the analyte vapor is doubled. Excellent detection limits with absolute masses of 0.1 pg Cd have been obtained.

Kitagawa et al.[46] used a graphite furnace in a Faraday configuration with Glan prisms and obtained detection limits of 0.5 pg Cd (5 $\mu\ell$), 20 pg Ag, and 30 pg Cu.[51] Magnetic line-crossing effects due to the hyperfine and isotopic structure, as discussed in Section III.B, could be suppressed by broadening the source line in pulsed lamp operation at higher

power. The effect of broadened source lines has been demonstrated with the determination of Sb, Bi, Ag, and Cu.[65]

The effect of CFS is restricted to resonance lines of the anisotropic vapor. Jolly and Stephens[73] presented an apparatus for "nondispersive" multichannel multielement determination. Measurements without monochromator and without any other spectrally resolving device are possible, due to the good suppression of unspecific off-resonant intensity by CFS. They coupled their photomultiplier by a light guide directly to the Glan-type polarizer. With flame atomization and with six lamps containing the elements Ca, Cr, Cu, Mg, Ag, and Na operated in a pulsed mode with each lamp cyclically focused into the detection channel, simultaneous multielement determination was realized.

The characteristic data, obtained in single- and multielement mode, are compared with the results of AAS measurements by means of the same flame and with the same analytical sources. In multielement operation, the CFS detection limits are roughly of the same order of magnitude as those of the AAS. However, detection limits for Na are obtained eight times better with CFS than with AAS. Spectral interferences were found from alloyed Ag in the Cr hollow cathode and from Mg in the Ca lamp. The authors succeeded with suppression of these interferences. In the single-element mode, with an interference filter in front of the detection channel, detection limits were obtained better predominantly with CFS than with AAS.

Hirokawa et al.[74] used a commercially available furnace unit with a graphite cuvette in Voigt configuration, a permanent magnet (Hitachi 170-5104/5105), producing a field strength of 1 T. They determined Li, K, Ca, Sr, Ba, Na, Mg, and especially Ag in aqueous solution and in the presence of high concentrations of lead, zinc, and copper.[74] Calibration characteristics for these measurements are presented in Figure 26. The presence of up to 10 μg Pb, 5 μg Zn, and 1 μg Cu has been tolerable for determination of 0.1 ng Ag. The influence of up to 100 μg Fe, Cu, Ni, and Na on the determination of 0.6 ng Pb is also likely low.[75] By ashing the sample at 550°C, the effect of nitric acid up to concentrations of 3% becomes negligible. Similar results have been obtained for the determination of Cu in steels, Zn, and Sn, and in the presence of Fe, Zn, Ni, Mn, Al, Pb, Ag, Mg, Bi, and Na.[76] With a lidded graphite-cup cuvette,[63] Cd and Zn have been determined by direct solid sampling in high-purity tin.

2. Simultaneous and Sequential Multielement Determination with Continuum Sources

As shown before, CFS may have certain advantages for particular analytical problems. However, the most interesting performance is real multielement determination, which can be carried out with continuum sources, as proposed by Ito,[26] Yamamoto et al.,[36] and Debus, Hanle, Scharmann, and Wirz.[28] Using a 450-W X3 lamp, in combination with two Rochon prisms and a monochromator with a photomultiplier for sequential multielement determination, in chopper-modulated operation with lock-in detection,[26] the detection limits given in Table 1 have been obtained. The corresponding limits for the AAS have been measured with the same apparatus, but with the respective single-element hollow-cathode line-sources. Thus, continuum cources CFS data are compared with line-source AAS data. The example of titan confirms that, in certain cases, CFS detection limits can be lower than those of the AAS even if line-source AAS data are compared with CFS data, which are measured with the low spectral intensity of continuum sources and with multielement capability.

The analytical capacity, promptness, and efficiency of a spectrometric approach is considerably increased in simultaneous operation. Simultaneous multielement determination in combination with ETA has been carried out by means of acoustooptic tunable filters,[70] vidicons,[34] or photodiode arrays.[29,77] Figure 27 shows the spectrum, measured simultaneously with a photodiode array by one single ETA of one sample of human hair, dissolved in nitric acid. Some calibration characteristics, which are obtained with this simultaneous multiele-

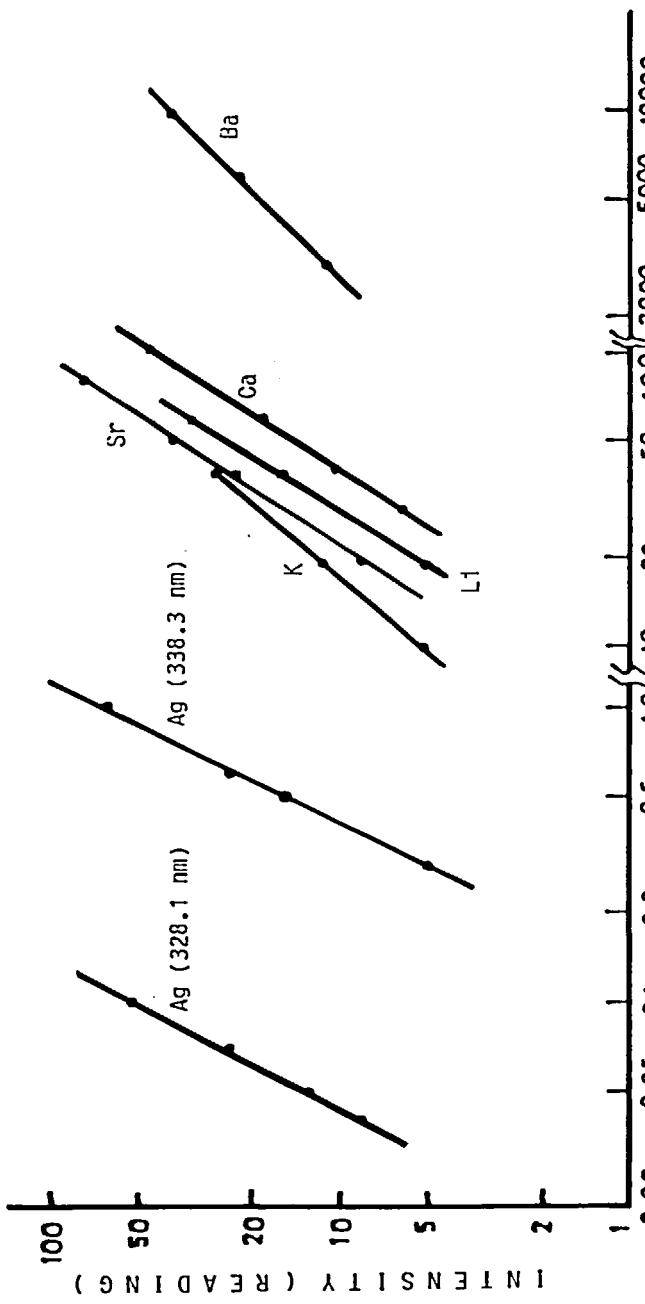

FIGURE 26. Calibration characteristics for Li, K, Ca, Sr, Ba, and Ag, measured with standard solutions of these elements in the presence of pure lead.[74]

Table 1
DETECTION LIMITS MEASURED BY MEANS OF THE SAME CONFIGURATION WITH GF-ETA BY CFS WITH A Xe CONTINUUM SOURCE AND BY AAS WITH HOLLOW-CATHODE LINE SOURCES[26]

		Detection limits (ppb in 10 μℓ)	
Element	Wavelength (λ/nm)	CFS (Xe continuum source)	AAS (hollow-cathode source)
As	197.2	500	5.0
Cd	228.8	0.6	0.02
Cr	357.9	7.0	1.5
Cu	324.7	7.0	0.5
Fe	248.8	13	0.5
Mn	279.5	2.0	0.2
Ti	365.4	140	200
V	318.4	50	20
Zn	213.9	1.0	0.05

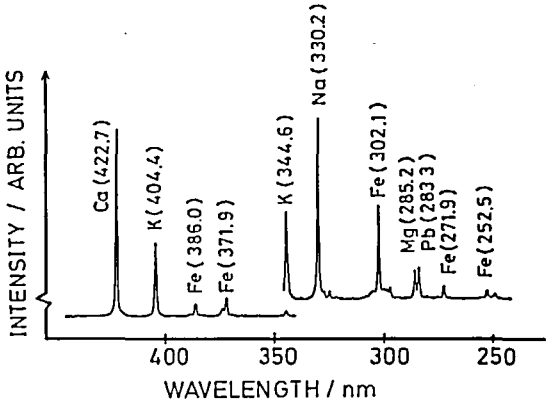

FIGURE 27. CFS spectrum of a dissolved sample of human hair measured simultaneously with a continuum source and a photodiode array (sample of 10 μℓ containing 300 μg human hair dissolved in nitric acid).[77]

ment technique, using a channel plate and a photodiode array,[44] are shown in Figure 28. The detection limits (0.6 ppb Cd/10 μℓ) for twice rms noise signal are already at the present and even with a home-made furnace[45,47] in the order of those previously measured in a sequential mode by a photomultiplier (Figure 21). The authors soon hope to be able to publish improved results, which are measured with a commercially manufactured furnace.[64]

Applications of CFS with continuum sources (150 and 450 W Xe) to determine Al, Cr, Cu, Fe, Mg, Mn, Mo, Ti, and Zn,[70] as well as yttrium, rare earths,[78] alkalines, earth alkalines, and many other elements,[49,79] all dissolved with dilute acids, have been presented by Hirokawa et al. The tolerable concentrations of acids are given as well as the tolerable concentrations of a table of interfering metals.

3. Analytical Experiences with Flames

Some fundamental work on CFS has been done with flames[43,44,52,73,80,81] which allow measurements with time constant atomization and give high precision of vapor densities.

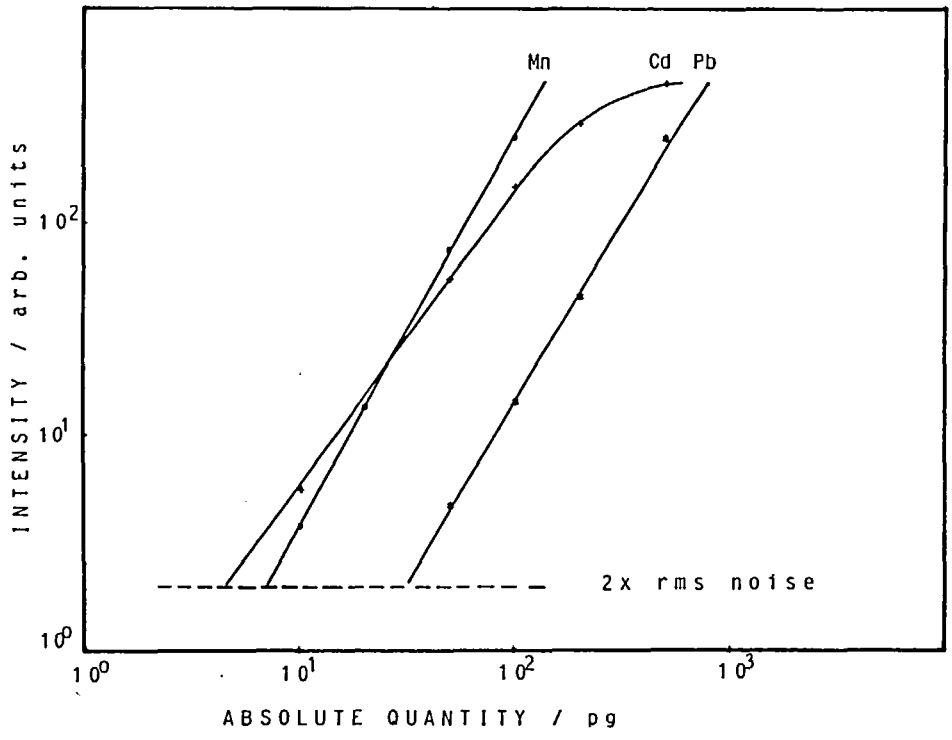

FIGURE 28. Calibration characteristics of some elements, measured with GF-ETA in simultaneous multielement mode with a Xe continuum source, a channel plate as optical intensifier, and a photodiode array.[44]

However, flames can be used as atomizers in analytical CFS too. As known from the AAS with flame atomization technique, the detection limits are up to three orders of magnitude higher in combination with flame atomization than with ETA. The apertures as well as the aperture angles of common flames are smaller than those of furnaces. These geometrical properties in connection with the low spectral radiant densities of continuum sources strongly reduce the CFS intensity transmitted at saturation maximum. However, the effect of lower line intensities can be compensated partly by longer detection times, higher precision, and reduction of background and noise. Thus, CFS in combination with flame atomization allows multielement determinations of high accuracy.

Figure 29 presents calibration characteristics of the CFS line intensities for the elements Ca (422 nm), Cu (324 nm), Cr (359 nm), Mn (403 nm), and Ni (341 nm) obtained with flame atomization.[43,44] These characteristics follow with high accuracy a square law. Furthermore, calibration characteristics of Ca and Cr are given for a single vapor transit of the probe light as well as for a seven-pass mirror contribution (see Section VI.C). Figure 30 shows a CFS apparatus with flame atomization for sequential multielement determination using a 450-W Xe source, and with polarizers of the Glan-Taylor type. The instrument has been constructed for determination of the elements Na, K, Ca, Al, Mg, Fe, and Mn in drinking water in a single sequential measurement.[82,83] It is a low-cost spectrometer which offers multielement operation with a very small monochromator of 12.5 cm focal length, with only one single long-living light source and a photomultiplier as detector.

Kersey and Dawson[48] investigated CFS detection limits for flame atomization of the elements Ag, Cu, and Mg. Hollow-cathode lamps have been used as well as a 15-W continuum spectrum D_2 lamp.[66] Detection limits, obtained by different approaches, are given in Table 2. In combination with hollow-cathode sources, approaches of optical linearization

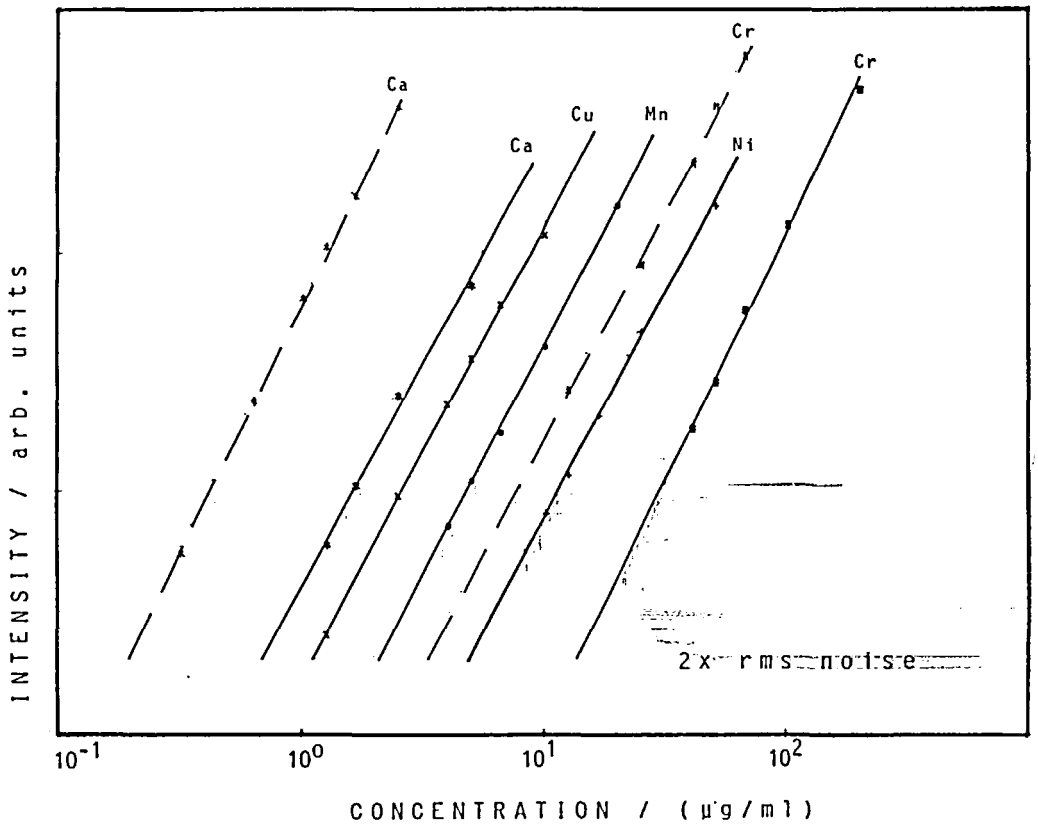

FIGURE 29. Calibration characteristics for continuum source CFS line intensities of the elements Ca (422 nm), Cu (324 nm), Cr (359 nm), Mn (403 nm), and Ni (341 nm) obtained with flame atomization in Voigt configuration (unbroken lines: one single vapor transit of probe light; dashed lines: seven-pass mirror configuration; see also Section VI.C).[44]

(see also Section VI.B) have been applied with an improvement of detection limits up to an order of magnitude.

As known from AAS, optimum conditions for vaporization of different elements are realized with different gaseous mixtures and in different zones of the flame. Thus, experiences with detection limits, background, dynamic range, and precision of flames in comparison with GF-ETA cannot be generalized from one element to each other. However, in absence of a high temperature furnace, continuum background of flames is generally lower than in ETA technique. Interferences due to foreign light and weak contributions of emission lines can be corrected, in principle, by techniques of modulation of the source light or of the magnetic field. However, detection limits are mainly two or three orders of magnitude higher with flames than with ETA.

Without this correction, specific emission may change the calibration characteristics slightly in the concentration range near the detection limit. If the detection limits of flame emission spectroscopy are lower than those of CFS, this additional contribution of flame emission can be used for an expansion of the detection range. Since it contributes with linear slope to the total detected intensity (I) as a function of the concentration (c), the calibration has to be corrected as shown by Equation 55:

$$I = ac^2 + bc \tag{55}$$

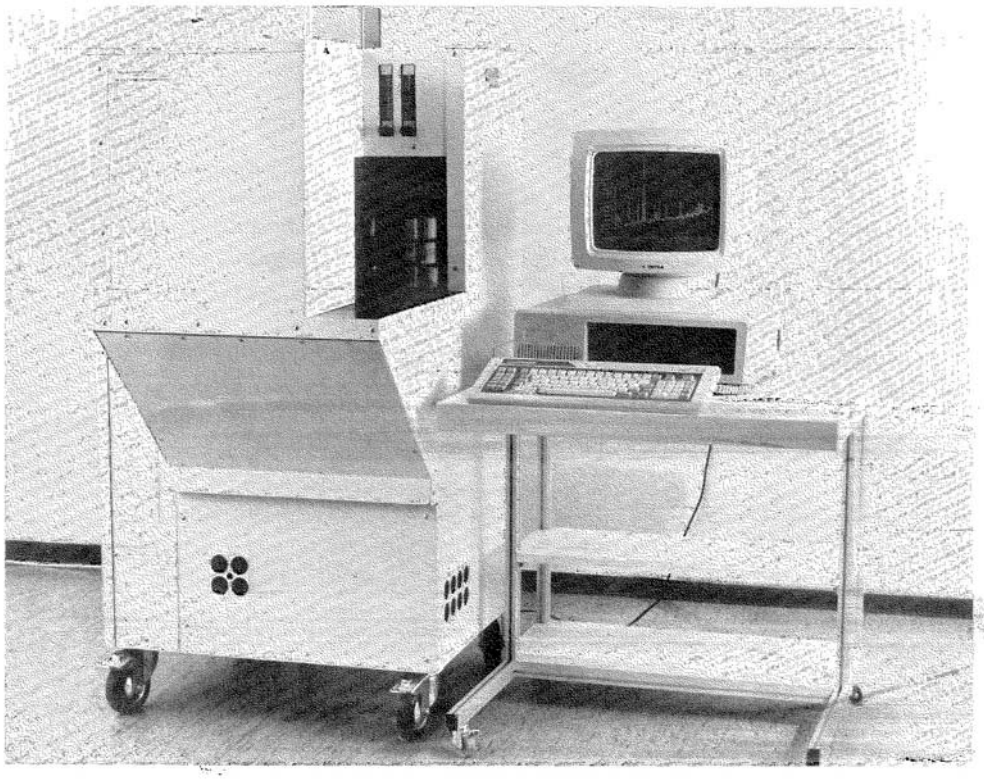

FIGURE 30. CFS apparatus with flame atomization for sequential operation with a monochromator (12.5 cm focal length) and a photomultiplier.[83]

Table 2
COMPARISON OF DETECTION LIMITS OF AAS AND CFS OBTAINED WITH FLAME ATOMIZATION AND HOLLOW-CATHODE SOURCES AND CROSSED POLARIZERS (CP) AS WELL AS POLARIZER OFFSETS (PO)[48]

Element	Wavelength (nm)	Detection limits (μg/mℓ) AAS	ZAAS	CFS (cp)	CFS (po)
Ag	328.1	0.10	0.15	1.78	0.14
Cu	324.7	0.21	0.39	2.14	0.15
Mg	285.2	0.046	0.130	0.416	0.183

A computer-controlled instrument will make use of any opportunity to expand the concentration range by combining flame CFS and emission measurement. Furthermore, a computer-controlled apparatus will calculate automatically the calibration constants b and a by calibration measurements without and with the external magnetic field. With these calibration constants, the corrected concentration c in the expanded calibration range is determined (Equation 56):

$$c = \sqrt{(I/a + b^2/4a^2)} - b/2a \quad (56)$$

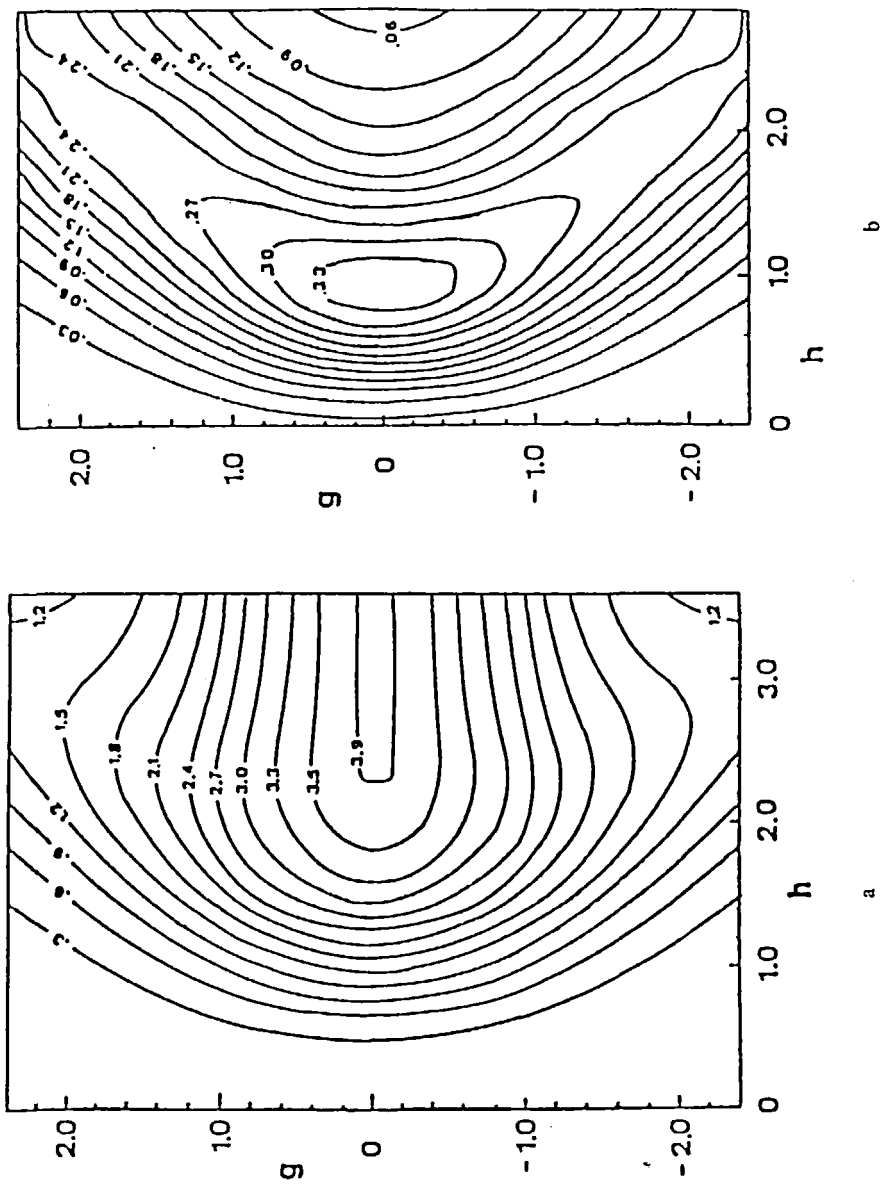

FIGURE 31. Contour map of the CFS intensity as a function of relative magnetic field $h = \gamma B/\Delta$ and of the relative detunig $g = (\omega_s - \omega_o)/\Delta$ of the source line from the atomic line center. (a) Faraday configuration. (b) Voigt configuration.[35]

In inverse Zeeman AAS,[84] CFS interferences due to paramagnetic molecules may be observed. As discussed in Section VII.A, contributions of molecular CFS are very weak. Thus, only molecular contributions of high concentrations as from OH^- in flames are observed.

VI. OPTIMIZATION AND IMPROVEMENT

A. Field Configuration and Strength

Optimal conditions of magnetic field configurations and strengths are discussed by many investigators. Most authors deal with the problem of field optimization in combination with line sources[26,46] of different line width.[66] A very detailed discussion is given by Kankare and Stephens[35] in "A Unified Theory of Magnetooptic Phenomena in Analytical Atomic Spectroscopy". The CFS resonance interaction of atomic vapors is studied under conditions of Gaussian broadening as well as Lorentzian broadening, with line sources, and in Faraday and Voigt configurations.

For Gaussian resonance line profiles, normal Zeeman effect, and a Faraday configuration, the optimum magnetic field strength is roughly about $B_{opt} \approx \Delta/\gamma$, i.e., the splitting of the σ components is about twice the Gaussian parameter Δ. Figure 31a shows a contour map of the CFS intensity as a two-dimensional function of relative magnetic field $h = \gamma B/\Delta$ and of the relative detuning $g = (\omega_s - \omega_o)/\Delta$ of the source line ω_s from the atomic resonance ω_o. The respective contour map for the Voigt configuration is given in Figure 31b. The signal intensity as a function of magnetic field is known as the zero-field line-crossing profile (Equation 39). The intensity of a line source, transmitted by a Voigt configuration, increases with the fourth power of h (Equation 49), its maximum about 15% higher, but with a broad optimum at a relative field strength $h \approx 3$, $B_{opt} \approx 3\Delta/\gamma$, i.e., the optimum field strength of a Voigt configuration is about three times higher than that of the Faraday configuration.

Additional calculations are carried out for the other limiting case of the plasma dispersion function, for the Lorentzian line profile, and for the Faraday configuration. The results are of the same order of magnitude as for the Gaussian limit. If related to equal half-width, optimum field strengths differ within about 50%, and those for the maximum transmitted intensity differ within about 15%. However, these calculations have been carried out for line sources. An estimation confirms that a finite source line width changes the optimum parameters only very slightly.

This conclusion is very roughly valid for CFS in combination with continuum sources, too.[26] Calculations and measurements[71] of spectral contributions of the CFS line profiles show the respective Lorentzian- or Gaussian-like Voigt profiles at low particle densities. However, there is a strong dependence on the related case of Lorentzian or Gaussian broadening of the Voigt profile in the range of CFS saturation.[85,86] Figures 10 and 12 show the transmitted line profiles of a Voigt configuration in the case of the Gaussian limit.

Thus, optimum field conditions in general depend on the line structure,[51,52] line shape and line width, and the splitting pattern of the respective element as discussed before. In principle, higher field strengths are required in Voigt configurations than in Faraday configurations. Furthermore, optimum field strength increases with increasing line width. Caused by the square-law characteristic, any line broadening, whether due to atomic collisions, Zeeman effect, field inhomogeneity, molecular vibration-rotation structure, or isotopic or hyperfine structure, causes a reduction of the total CFS signal intensity and, thereby, an increase of the CFS detection limits. Line-crossing effects may cause relative optima at lower field strengths.

However, and especially in combination with continuum sources, optimum conditions are represented mostly by very flat maxima. Quite satisfactory conditions can be realized with a constant magnetic field strength of about 0.8 to 1 T in a Voigt configuration. The optimum is attained at a higher strength. Thus, permanent magnets are suitable.[49] The field strength

can be reduced even more by using a Faraday configuration. However, despite the slight advantages of the Faraday configuration, the Voigt configuration is the easier construction. In particular, flame burners of the required nozzle length are difficult to combine with Faraday configurations.

B. Optical Linearization

CFS is a method of polarization spectroscopy, and thus a special form of interference spectroscopy. Under conditions of exactly crossed polarizers, the intensity follows a square-law characteristic. Thus, as furthermore known from polarization and interference spectroscopy, the signal can be linearized by a finite phase shift of the interfering waves, i.e., by a finite angle of polarizer uncrossing or by a birefringence phase shift, respectively.[87]

Optical linearization by offsetting the passive polarizer-analyzer system and its effect on sensitivity, detection limits, and signal-to-noise ratio has been investigated by Stephens,[88,90] Stephens and Kankare,[89] and Kersey et al.[48,66] Depending on the field configuration and the shift of the source line with respect to the center of the atomic resonance line, linearization can be optimally achieved by an angular offset of the polarizer-analyzer system or by a phase retardation. If the source line is centered to the atomic resonance line, a Voigt configuration works primarily by rotation of a mainly linear polarization via dichroism, while the Faraday configuration is also rotating a mainly linear polarized radiation via Faraday effect. Thus, in both cases, simple offset angled orientation of the polarizers is optimal for optical linearization in combination with line sources.

Linearization of the CFS signal may be favorable if time-resolved detection and integration of time-resolved measurements are required. However, for a modern computer-operated apparatus, linearization of any characteristic of signals or spectra will not be a problem at all. Thus, linearization of the square-law CFS signal before detection by itself means only reduced slope of the characteristic and not a great advantage for a computer-controlled apparatus.

On the other hand, the signal is increased by optical linearization. Thus, polarizer uncrossing allows signal-to-noise improvement. In particular, the ratio of the signal to any unspecific intensity such as from incomplete polarizer extinction, furnace or flame emission, as well as foreign light can be increased. Thus, the signal-to-noise ratio is increased with respect to all background noise, whether of unspecific intensity or of photodetectors and amplifiers. However, reduction of signal-to-noise ratio can be obtained by atomic absorption and by increasing transmission of flicker noise from the source, while signal-to-noise ratio due to the signal fraction of photon shot noise is proportional to the root of the transmitted intensity and remains in a constant order of magnitude.

Figure 32 shows the signal-to-noise ratio of CFS as a function of the polarizer offset angle for different extinction ratios, calculated by Stephens and Kankare.[89] Optimized polarizer uncrossing causes interesting signal-to-noise improvement and efficient reduction of detection limits. Optimum offset angles can be determined as a function of unspecific intensity, i.e., mainly of the polarizer extinction ratio and background intensity. Table 2 gives a comparison of detection limits measured by flame atomization with crossed polarizers (cp) and optimal polarizer offset (po).

Nevertheless, these approaches of angular polarizer offset-rotation are only working in combination with line sources. In combination with continuum sources, dispersive and dichroic contributions in different spectral ranges of the atomic resonance line are compensated. This is also valid for any complex polarizer uncrossing by combinations of angular polarizer offset and phase retardation as long as this uncrossing is constant within the spectral line profile. Linearization by dispersive polarizer uncrossing is presented.[91]

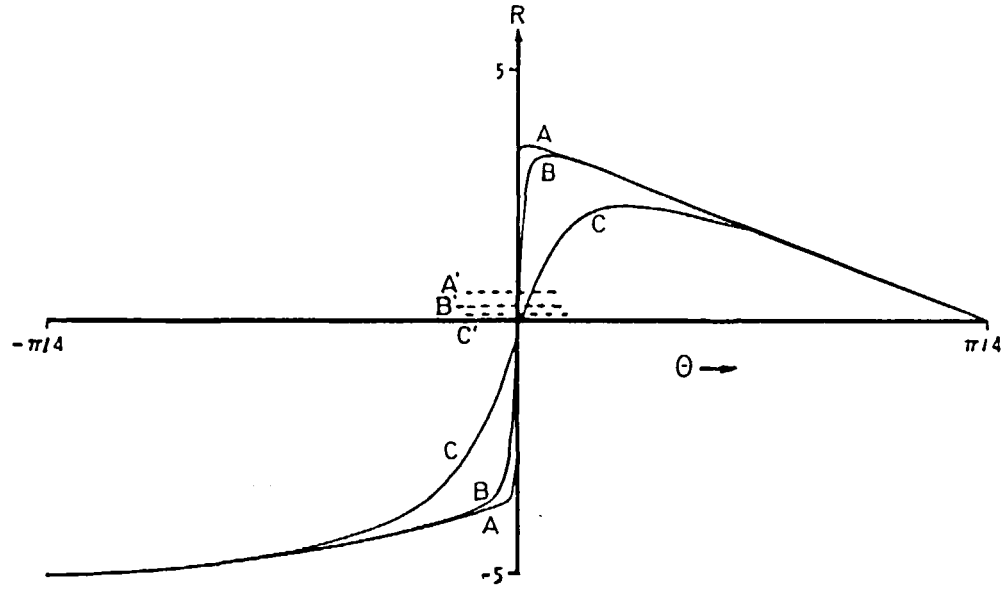

FIGURE 32. Calculated signal-to-noise ratio R of the CFS signal as a function of the polarizer offset angle (dichroic absorbance of Voigt effect $a_\pi = 10^{-3}$; A, B, C: polarizer extinctions = 10^{-6}, 10^{-4}, 10^{-2}).[89]

C. Multiple-Pass Mirror Configurations

1. Fundamental Considerations

The length of the atomic interaction zone enters the CFS intensity (Equations 39 and 40) by the product $(f_{e,g} \cdot n_A \cdot L/\Delta)^2$ together with the oscillator strength $f_{e,g}$ describing the strength of the line, the atomic density n_A, and the line width. Thus, the length of the optical path is represented by the sensitive square-law term, like the atomic density. Multiple-pass configurations, based on reflector systems, allow the multiplication of this interaction length and may spare one polarizer in certain configurations.

In a planar model of a focal two-mirror system, an optical ray can be described by its axial separation x and its axial angle α at the entrance, i.e., by the dimensionless vector s = (x/L, α) (L = mirror separation). After one transit and after one reflection at the opposed focal mirror with the focal length f, this ray is described by s′ = (x′/L, α') and can be expressed by means of the matrix A:

$$\mathbf{s}' = \mathbf{A}\mathbf{s}$$

$$\mathbf{s}' = \begin{pmatrix} x'/L \\ \alpha' \end{pmatrix} = \begin{pmatrix} x/L + \alpha \\ \alpha - x'/f \end{pmatrix} = \begin{pmatrix} 1 & 1 \\ -L/f & 1 - L/f \end{pmatrix} \begin{pmatrix} x/L \\ \alpha \end{pmatrix} = \mathbf{A}\mathbf{s} \qquad (57)$$

Optimum transmission from the entrance aperture to the output aperture of a multiple reflection system is achieved after n reflections, if the ray is reproduced, forming an image of the entrance mirror on the output mirror:

$$\mathbf{A}^{n+1} = \begin{pmatrix} 1 & 1 \\ -L/f & 1 - L/f \end{pmatrix}^{n+1} = \begin{pmatrix} \pm 1 & 0 \\ 0 & \pm 1 \end{pmatrix} \qquad (58)$$

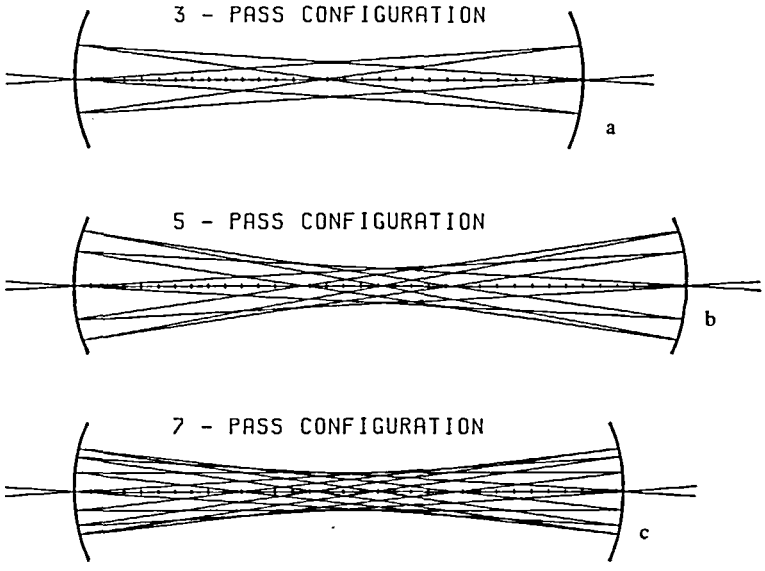

FIGURE 33. Multiple-pass mirror configurations: N + 1 = 3 (a), 5 (b), and 7 (c) vapor transits.[43]

An odd number of reflections n means an even number n + 1 of transits and detection backward in reflection with the necessity of separation of the CFS intensity from the input radiation by a beam splitter. In particular, by use of a beam-splitting polarizer, a separate analyzer can be spared. Even n characterizes a configuration of straight forward detection. For a given number of vapor transits n + 1 and the related number of reflections n, Equation 58 has n solutions for the required focal length f.[43] These solutions differ in the number of crossings of the rays through the axis of the mirror configuration, which may be 1, 2, . . . n. Three favorable examples of multiple-pass configurations are presented in Figure 33.[86] Light entrance and exit is realized by holes in the mirror centers. The given examples with three and five transits are also characterized by three and five axial crossings of the optical rays. However, the last example of a seven-transit configuration is characterized by only six crossings of the axis. In this configuration, the fourth transit is parallel to the axis without crossing it.

2. Analytical Effect

Calibration characteristics and detection limits of forward configurations (even n) have been investigated for different types of solutions of Equation 58 in combination with a flame atomizer.[43,86] These measurements, with the low aperture and low aperture angle of flames with single-slot burners, show that optimal configurations are realized, preferring long ray paths in the close-axis range. Thus, for a given high number of transits, a configuration with a lower number of ray crossings through high vapor density in the axial flame center, but with ray angles closer to the axis, may have advantages in comparison with a higher number of axial crossings, but with greater mean aperture angles (Figure 33c, with the fourth transit parallel to the axis).

Figure 34 presents examples of calibration characteristics, obtained for Cu without and with focal mirror configurations with n + 1 = 1, 3, 5, 7 transits. Improvement of detection limits has been obtained by about a factor of four. It demonstrates the high efficiency of intensity coupling by image formation from the input hole of the entrance mirror to the output hole in the center of the exit mirror.

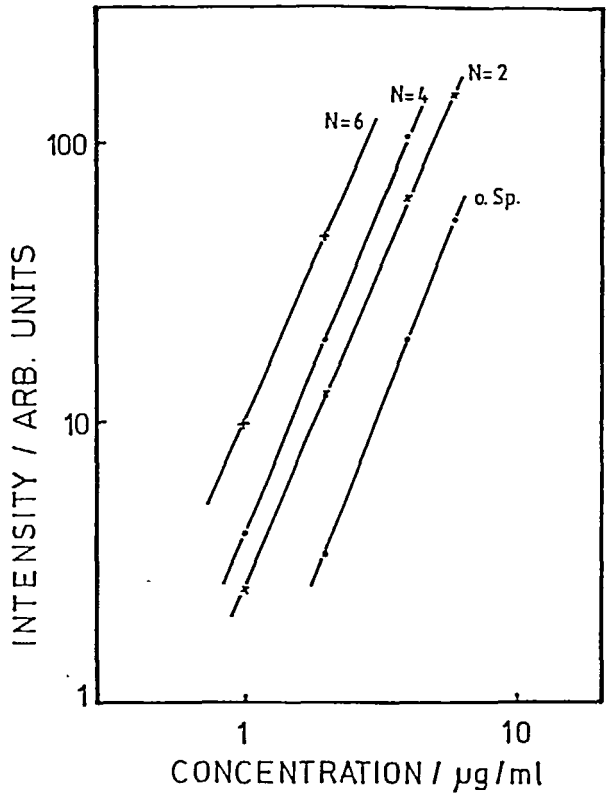

FIGURE 34. CFS calibration characteristics of copper (λ = 324.7 nm), measured with flame atomization, with a N + 1 = 3, 5, 7 pass configuration.[43]

In principle, a similar effect of a multiple-pass configuration would be found in combination with the AAS, too. However, using CFS, reflection losses (1 − R) only contribute with the linear number of reflections n, i.e., ~(1 − R^n), while the signal increases with the square of the pathlength, i.e., with the square of the number of transits $(n + 1)^2$. Thus, total losses of 60% enter the analytical signal with root of the intensity while, due to the square-law effect of the light path, the primary CFS intensity of a seven-pass configuration is increased by a factor of nearly 50 (i.e., 5000%), resulting at least in an increase of the total output intensity by a factor of 16. Thereby, the signal-to-noise ratio is increased and the detection limit is reduced by about the given factor.

VII. BACKGROUND AND BACKGROUND CORRECTION

A. Inherent Background Properties

CFS is characterized by a combination of properties which inherently reduce the influence of optical interferences.

As discussed in Section IV.A, CFS is a zero method and the signal is generated directly by means of the optical polarizer configuration. In the alternative atomic resonance interaction technique, AAS, a small absorption signal, I_o-I_t is generated by measuring I_o and I_t. If the characteristic mass is detected, both of these intensities are 100 times higher than the absorption signal. With background compensation, as by ZAAS, I_t and I_o are detected in time sharing during different times by modulation and lock-in detection. By these means,

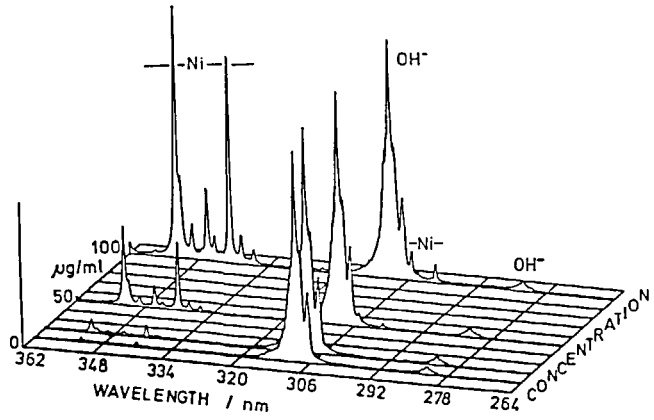

FIGURE 35. Flame atomization-detected CFS spectrum showing two OH^- bands.[43]

the ZAAS signal is furthermore reduced with the detection time while noise is added up incoherently from both measurements. The CFS signal is generated by optical subtraction (i.e., interference) of two radiation fields which coherently cover, e.g., the same flicker noise and detector noise from exactly the same time intervals (see also Figure 20).

Under ideal conditions and complete polarizer extinction, the detected intensity is reduced to the signal intensity. Thus, the source noise is reduced to its fraction related to the transmitted spectral signal, too. By the same reason, the photon shot noise is given only by the statistic of the signal and not by the absolutely higher fluctuations of the total basic intensities I_o and I_t (however, due to the lower total signal intensity, the signal-to-photon-shot-noise ratio is of the same order of magnitude as that of the AAS). Furthermore, the lower signal intensity $I_{CFS} \approx (I_o - I_t)^2/I_o$ can be detected by a detector with higher sensitivity.

Structured and unstructured background absorption share only with the detected spectral intensity I_{CFS} and not with the total transmitted intensity. Consequently, unspecific absorption of 1%, which equals the specific absorption of the characteristic AAS concentration, will be mostly within the limits of error by using CFS. By the same reason, due to the direct optical reduction of the intensity to the signal intensity I_{CFS}, and in spite of the square-law response, the dynamic range of CFS (i.e., the concentration range) is still high. Under real conditions, the advantages of a zero method extremely depend on the suppression of foreign light and on the quality, mainly on the extinction of the polarizers.

The effect of CFS caused by molecules is very weak. Due to the rotational angular momentum, the gyromagnetic ratio of molecules γ is generally lower than that of atoms. Thus, molecular CFS is mostly far from saturation of the molecular zero-field line-crossing profile. Furthermore, the oscillator strength of a molecular transition is distributed over the width δ of a generally broad molecular vibration-rotation band. Therefore, molecular CFS contributes very weakly proportional to $(\gamma B_o/\delta)^2$, i.e., the total molecular CFS intensity, which is given by the square sum of all vibration-rotation contributions of molecules, is extremely reduced in comparison with the intensity of molecular emission lines. However, molecules or molecular ions of very high concentrations as OH^-, mainly in the outer regions of flames (typical density 10^{15} to 10^{16} cm^{-3}), contribute real molecular CFS bands. Figure 35 shows the spectrum of a Ni solution with a strong OH^- band at 310 nm and a weaker band at about 282 nm wavelength.[85,86] Stronger interferences of this structured CFS background are given on the Zn (307.6 nm) line and the Pb (283.3 nm) line.

Using continuum sources, unspecific light contributes a very smooth spectral profile to the baseline of the detected spectrum. Such unspecific light from the source may be trans-

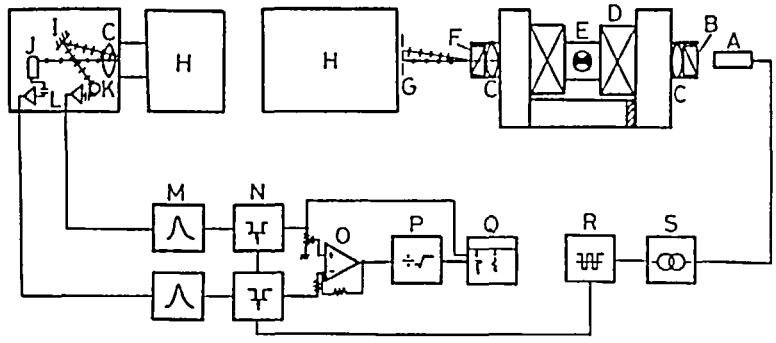

FIGURE 36. Schematic diagram of an CFS apparatus in Faraday-configuration ETA (D, E) with background detection by a beam-splitting Rochon polarizer (F) and correction by an analog circuit (O, P). A: hollow-cathode lamp; B: Glan prism; H: prism monochromator; J, K, M: detectors with bandpass preamplifiers; Q; recorder; N, R, S: synchronous gating electronics.[68]

mitted due to incomplete polarizer extinction and due to slightly anisotropic optical components, such as windows, mirrors, and lenses, or to scattering. The same is valid for furnace emission. Thus, as known from the emission spectroscopy, background intensity can be determined from the out-of-line intensity, which is given by a mainly smooth base line profile. Consequently, noise contributions of the background intensity can also be reduced by fitting and averaging the background profile over a certain spectral range.

CFS is based on a square-law effect. This means that, with respect to background, the spectral effect of changes of concentrations is dynamically expanded. On the other hand, the relative analytical effect of all spectral interferences, of absorption as well as emission, and of foreign light, structured molecular background, and all contributions of noise, including detection and signal processing, is dynamically compressed by a factor of two.

However, changes of the analyte atomic density, caused by the limited precision and finite fluctuations of sample feeding and atomization, enter the CFS intensity as the specific signal square law expanded and, therefore, with linear analytical effect. If the detection is carried out by signal integration without time resolution, results represent the root mean square of the atomic density. In time-resolved measurements, any weighting of the averaging process is possible with analog circuits or numerically with digital data.

Direct generation of the signal, without modulation and phase-sensitive processing, is an optimal condition for real time-resolved detection. Time-resolved spectra allow identification of matrix interferences, which cause double peaks, and allow to recognize time-dependent changes and fluctuations. Time-resolved measurement of the signal as well as background is of great importance for background correction in combination with ETA. In addition, time resolution is improved by square-law response. On the other hand, direct signal generation offers remaining options of time-sharing approaches by chopping or modulation and phase-sensitive measurement for simultaneous multielement determination[73] and background detection.[92-94]

B. Background Detection and Correction

Correction of background due to absorption of CFS intensity can be achieved by measurement of both polarization components $I_{\parallel}$ and $I_{\perp}$ transmitted by a beam-splitting polarizer such as a Rochon[68,69] or a beam-splitting Glan prism. The beam-splitting polarizers have been placed in front of the monochromator entrance or behind the dispersive element. A schematic diagram of a typical experimental configuration is shown in Figure 36. By generating the ratio $I_{\perp}/I_{\parallel}$ or the root $\sqrt{(I_{\perp}/I_{\parallel})}$ with an analog circuit and time integration, the

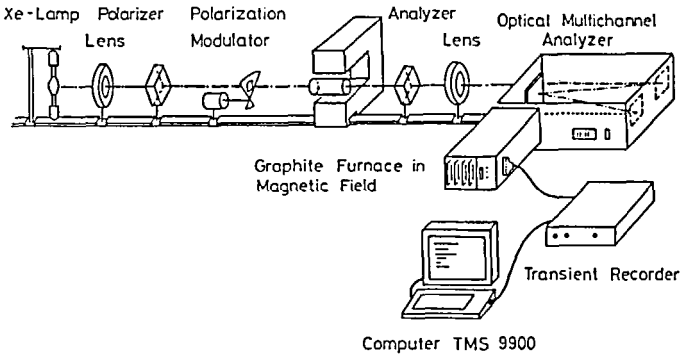

FIGURE 37. Arrangement of a continuum source ETA CFS apparatus in Voigt configuration for simultaneous multielement determination with background detection.[92]

analytical signal is created. Measurements of both polarizations have been carried out in static d.c. detection and in time-sharing operation with a rotating prism.[95] Determinations of Cd (228.8 nm) in aqueous solutions and starch as well as of Pb (283.3 nm) by direct solid sampling in orchard leaves, human blood, and volcanic ash demonstrate that the system is suited to overcome background absorption as well as specific atomic absorption.[46]

Modulation of the source light allows suppression of foreign light as from the graphite furnace. In addition, all kinds of unspecific intensity, foreign light as well as unspecific source light, can be detected by modulation of the magnetic field. If the magnetic field is switched off, the atomic vapor is isotropic, while the intensity transmitted by CFS is zero, background intensity can be detected.

In addition, the polarizer-analyzer system can be modulated in two dimensions. Synchronous rotation of the crossed polarizer-analyzer pair with respect to the magnetic field makes a similar effect as modulation of the field and allows the detection and correction of background intensity. However, the advantage of polarization modulation is that switching or modulation of a high-power-supplied magnetic field is unnecessary.

Furthermore, the polarizer-analyzer system can be modulated between positions of more or less uncrossing by angular rotation of the planes of polarization with respect to each other or by phase retardation or modulation of the degree of polarization. These approaches, as well as the detection of both directions of polarization with beam-splitting polarizers, allow the determination and correction of absorption background.

In combination with a continuum source, detection of background due to unspecific absorption has been demonstrated by modulation of the degree of polarization.[92-94,96,97] The principle of this apparatus is given in Figure 37. It shows a Voigt configuration set up with an additional stepping motor-driven chopper. The chopper disk consists of two shutter masks with a stress-birefringent silica plate in between. The masks interrupt the optical path while the diode array is read out by the computer; thus, the detected signal spectra are separated from the background spectra which are obtained when the silica plate is turned into the optical path.

The detector is controlled by a transient recorder which stores up to 16 time-resolved CFS signal spectra and transmission background spectra. Using an interpolation function for the time-dependent transmission, which is represented by a difference of two complex exponentials, efficient background correction has been achieved by measurement of only four time-resolved background transmission spectra. One of these background spectra, representing the asymptotic behavior of the transmission, is recorded before the atomization process is started. Three other transmission spectra are measured interspaced between the

signal spectra. The line intensity has been corrected with respect to the background absorption by dividing the intensity I(t) by the interpolated time-resolved transmission T(t). The square root of this corrected intensity represents the time-resolved analytical signal $S(t) = \sqrt{\{I(t)/T(t)\}}$.

Cadmium added to 1:5 diluted human blood has been used as a test sample (10 $\mu\ell$). Without a matrix modifier, the sample has been pretreated at a temperature of 300°C; thus, due to incomplete pyrolysis, a lot of smoke is developed while the atomization of Cd is beginning. Therefore, the determination of Cd is covered by unspecific absorption of up to more than 90% at maximum. Figure 38 shows the time-resolved 326.1-nm line of 2 samples containing the same masses of Cd, one with blood (Figure 38a) and one in pure aqueous solution (Figure 38c). In addition, the four values $T_0 \ldots T_3$ of the total transmission, detected at the same wavelengths, are presented with the interpolation function beside the time-resolved line intensity (Figure 38b). Figure 39 gives the complete spectrum of the sample of diluted blood about 1 sec later at a higher furnace temperature.

In consequence of the limited UV transmission of the experimental alignment, the 326.1-nm triplet-intercombination line of Cd had to be used, which is very weak in comparison with the strong 228.8-nm singulet line. By that reason, absolute masses of 25 to 100 ng Cd have been determined. The efficiency of the background correction system has been demonstrated by determination of different amounts of Cd added to human blood as well as in pure aqueous solution, with the same calibration by the aqueous standard solutions. As shown in Figure 40, the analytical signal, obtained with Cd in blood, rises later in time but higher than with pure aqueous samples. However, the areas under the time-resolved analytical signals agree within the limits of error given by the standard deviations.

Figure 41 shows the analytical signal, given by the area of the time-resolved square root of the background-corrected line intensity $s = \int S(t)dt = \int\sqrt{[I(t)/T(t)]}dt$, as a function of the cadmium concentration for cadmium with blood as well as of the same masses in aqueous solution. It demonstrates good agreement in the full concentration range of this calibration characteristic.

VIII. PERSPECTIVES

A. Detection Limits

In general, detection limits are reduced via suppression of background intensity and thereby background noise by polarization spectroscopy. Furthermore, reduction of intensity by suppression of basic intensity allows the application of more sensitive detectors as photon-counting systems. However, due to the square-law characteristic, the CFS intensity decreases with a higher slope with decreasing concentration. As shown in Section VI.B, this characteristic can be optically linearized. Using efficient optical equipment (powerful polarizers, etc.), detection limits of the zero-method CFS are expected to be generally lower than those of the difference-method AAS, especially of the ZAAS.[48] This is valid if the same line sources are used for CFS and AAS. Comparison of CFS detection limits by means of the very attractive continuum sources with multielement capability with those of AAS in combination with line sources mainly confirms lower limits for measurements with line sources. This fact is related to the higher spectral intensities. However, as shown by Ito[26] with the example of titan, certain detection limits of CFS, even in combination with continuum sources, may be better than those of the AAS with line sources.

Detection limits of all common spectrometric approaches have been improved, since analytical spectrometry is applied. Thus, detection limits of CFS have been and will be furthermore reduced, too. Table 3 shows examples of detection limits for determination of Cd in GF-ETA and of Cu in flame atomization technique. It shows improvement of the analytical capability. Detection limits in the favorable multielement operation are getting closer to the limits which previously were restricted to single-element methods.

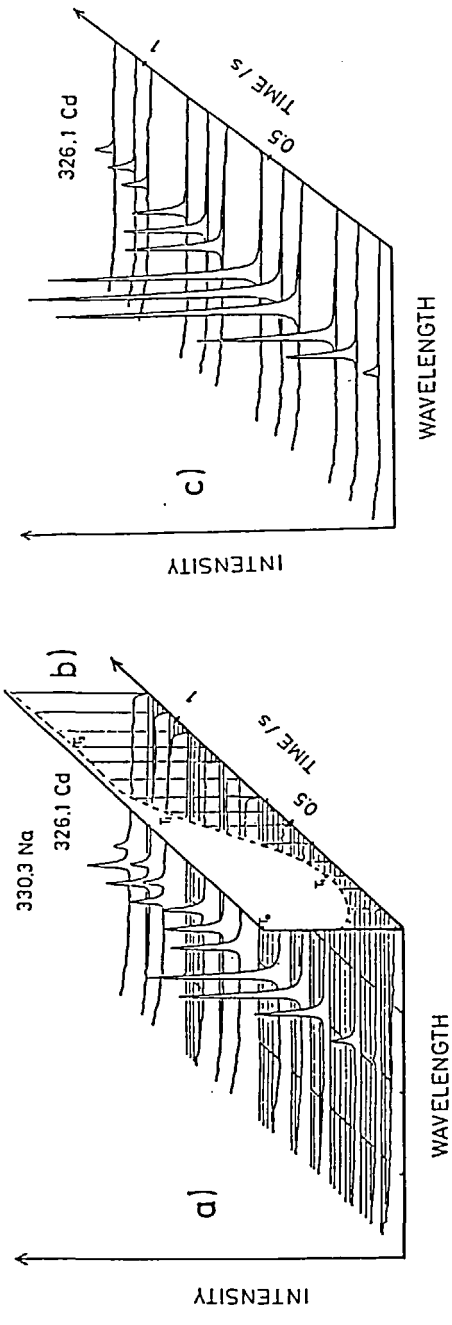

FIGURE 38. (a) Time-resolved resonance line (λ = 326.1 nm) of 100 ng Cd added to 10 μℓ of 1:5 diluted human blood. (b) Time-resolved measured transmission values and interpolation. (c) The same measurements as (a) with the same quantity of Cd, but in a sample of 10 μℓ pure aqueous solution.[92]

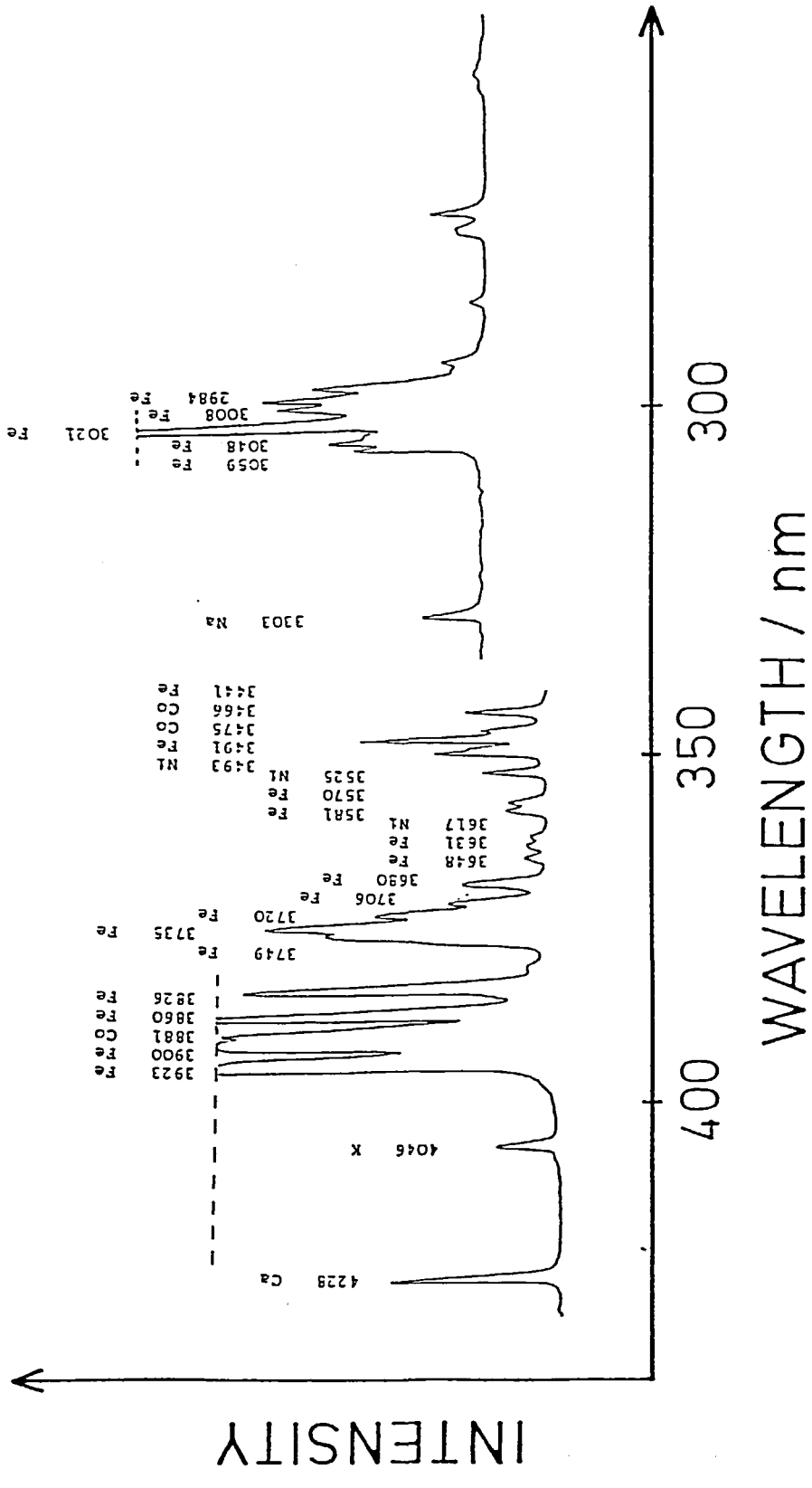

FIGURE 39. CFS spectrum of 10 µℓ of 1 : 5 diluted human blood, measured about 1 s after the spectra of Figure 38. The intensity of the left part of the spectrum with longer wavelenths is reduced by a narrower entrance slit.[93]

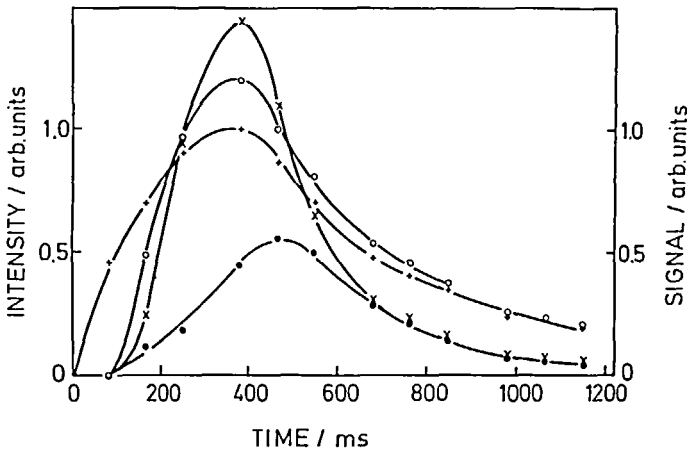

FIGURE 40. Time-resolved course of the uncorrected peak line intensity I(t) (•); Cd added to 5:1 diluted human blood of the corrected intensity I(t)/T(t) (x); corrected and linearized signal $\sqrt{(I(t)/T(t))}$ (o); and linearized signal of the same quantity of Cd in pure aqueous solution (+) (quantities as in Figure 38).[93]

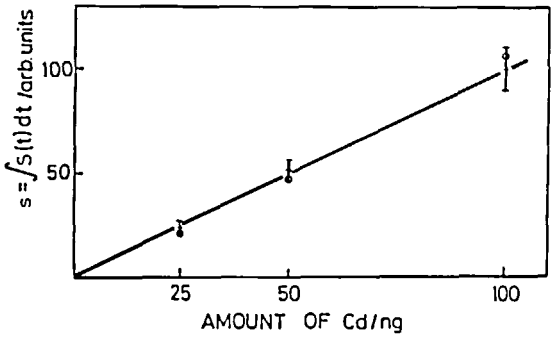

FIGURE 41. Peak areas of the time-resolved analytical signal S(t), given by the integral of the time-resolved square root of the background-corrected line intensity as a function of the concentration of cadmium added to 1:5 diluted human blood (+), as well as with the same concentrations in aqueous solution (o) (error bars giving the standard deviations).[92]

However, it also should not be ignored that many applications run into problems with determinations in the range of high concentrations. Dilution is often coupled with contamination of the samples and thus should be avoided as far as possible. Water analyses in drinking-water supply, by flame-AAS for determination of alkaline and alkaline-earth elements, are carried out mainly with burners operated in crossed position with respect to the optical path. With CFS, sodium concentrations up to 10 μg/mℓ are determined on the 589.0/589.6-nm doublet of sodium, and up to some milligrams per milliliter on the 330-nm line, before CFS is saturated. Table 3 furthermore confirms that detection limits with flames are typically up to three orders of magnitude higher in concentrations than with ETA.[100]

Increase of relative sensitivity by increased slope of the calibration characteristics is generally paid by a decreasing dynamic range, i.e., a reduced concentration range. However, due to other features, such as the feasibility of a zero method, the concentration range of

Table 3
DETECTION LIMITS OF CFS [Cd, 10 μℓ SOLUTION (IF NOT OTHERWISE NOTED)] FOR LINE SOURCE SINGLE-ELEMENT AND CONTINUUM-SOURCE MULTIELEMENT DETERMINATION IN SEQUENTIAL AND SIMULTANEOUS OPERATION

	Determination of Cd by GF-ETA (ppb)			Determination of Cu by flame (ppm)		
		Multielement			Multielement	
Year	Single element	Sequential	Simultaneous	Single element	Sequential	Simultaneous
1977	0.01[25]					
1978	0.1 (5 μℓ)[46]					
1980		0.6[26]				
1981		5[28]		0.15[a]—2[48]		
1983				0.5[98]		
1985						5[81]
1986			0.6[44,47]			0.25—0.9[b,44]
1987			0.4[47,94]		0.2[99]	

[a] Optical linearization.
[b] Multiple-poss mirror configurations.

CFS still remains quite high,[99] even the concentration range, which can be determined by one single line. Computer-controlled evaluation of lines of different strengths expands this concentration range extremely to higher concentrations.

B. Reproducibility

Xe and D_2 continuum sources are characterized by very constant light emission over long periods of time excluding many problems of spectral changes, fluctuations, and line inversion as known from the AAS with line sources. Furthermore, it is not involved with fluctuations of such various excitation conditions as emission methods, depending not only on the gas composition, atomic density, and gaseous temperature, but also on the electron density and electron temperature.

CFS systems with mainly spectral- and time-constant properties are well suited for long-time or permanent calibration. Furthermore, approaches of background detection and correction as described in Section VII.B include the measurement of efficiency and transmission of the entire optical system from the light source to the detector. Thus, calibration of the instrument is permanently corrected with respect to all components except the atomizer and sampler.

The reproducibility of atomizers has been improved by controlling temperatures and heating rates of furnaces as well as the parameters of the sheath gas atmosphere, and furthermore by use of matrix modifiers. Furnaces become more sophisticated with cups and boats, with differentiated functions of sample containment, pretreatment, atomization and probing, and pyrolytically coated surfaces and isothermal heating conditions.

By suitable monitor elements, which are not previously contained in the sample and are added in suitable concentrations, the atomization process can be permanently recalibrated. Thus, an increasing number of problems of element determinations and especially element monitoring might be solved with long-time calibrated or even permanently calibrated instruments. Probing by externally generated continuum spectrum radiation and background correction over all optical components offers favorable preconditions for long-time constant calibration.

C. Time Resolution

Memories and storing capacities, even of cheap computer systems, are getting so large that all information being measured with a sample can be stored easily and evaluated after all data are completely available. Thus, signals predominantly should be detected and recorded time-resolved and not integrated before final evaluation. Time-resolved ETA measurements make it easier to recognize matrix effects by structured peaks and double peaks. Spectral interferences can be realized by time-resolved measurement if elements are vaporized at different temperatures of atomization. The zero-method CFS offers optimum conditions for real time-resolved detection.

The square-law response further effects improved time resolution of CFS. Peaks, detected with a square-law sensitivity, are narrower and of sharper structure than with a linear detection characteristic. With respect to signal variations, the square-law detection is weighting predominantly phases of a high signal, resulting in a higher signal-to-noise ratio. However, this advantage is given up if the signal is integrated after square-root linearization and if peak integration is extended too far into signal decay. This problem can be overcome by approaches of integration over a limited time range, where the signal is sufficiently high, and by approaches of correction with respect to the suppressed remainder integral.

D. Computer-Controlled, Computer-Combined Approaches and Equipment

CFS with only one single and unproblematic continuum source is suitable for the determination of a large table of elements with detection limits that are reasonable for many requirements and, in certain cases, may exceed those of the AAS with single-element line sources. The multielement capability, mostly with a few lines per element, with different strengths, suited for different optimum concentrations and optional approaches of checking, with the additional option of line sources and the compatibility with approaches of absorption and emission spectrometry, will not be used with full power without computer-controlled operation.

A computer-controlled instrument will make use of several advantages of CFS background detection and correction, too. An optimal computer-controlled system will make use of the high relative sensitivity of the square-law characteristic as far as possible, but also will raise a weak signal over background noise by optical linearization. For special requirements, the continuum source can be automatically replaced by certain line sources for optional sensitive operation in a certain single-element mode. Thus, difficult determinations can be made, each under optimum conditions.

As shown before, spectroscopy of CFS can be realized by means of an apparatus that mainly conforms with an apparatus for inverse ZAAS. The principle difference is the additional polarizer-analyzer system, the approach of direct signal generation, and omission of formation of an absorbance signal by phase-sensitive rectification.

On the other hand, cheap and fast personal computers are well suited as controllers as well as intelligent data recorders. In combination with analog-to-digital converters or with photon-counting systems, such computers can be used as phase-sensitive rectifiers and for linearization of any calibration characteristics. Thus, CFS and digital approaches of phase-sensitive detection, installed by computer software, can be used as optional approaches for signal generation and signal-to-noise improvement. A computer-controlled CFS instrument includes all feasibilities of the ZAAS technique and the option on additional detection of light emission of flames or plasmas,[101] but with the additional possibility of resonance detection with direct optical signal generation by polarization spectroscopy. It includes the option on a broad-band continuum source, without loss of any opportunity, which line sources of certain elements might have.

For a given example, the computer program may provide the determination of all essential elements of a sample as well as elements where this standard lamp is advantageous or suited

by use of the continuum source. Nevertheless, the determination of a few other elements, for which line sources are preferable, might be automatically carried out by using certain hollow-cathode line sources. At least the determination of some other elements might be programed by means of AAS with parallel polarizer/analyzer orientation or by using the emission of a flame. Thus, different methods as well as different components can be combined in one apparatus — CFS, ZAAS, and OES — the multielement capability with continuum spectrum sources with certain line sources for special determinations. Optimized computer-controlled application of the variety of these facilities will improve versatility, detection limits, precision, reliability, promptness, and speed of optical spectrometric determinations.

E. Direct Solid Sampling

Graphite furnace atomization is appreciated as a powerful tool for direct solid sampling.[102,103] Sophistication of furnace constructions and experience in treatment of various matrixes for graphite GF-ETA is still proceeding.

As outlined in Section VII, CFS as a zero method with square-law response is characterized by favorable inherent background properties. Additional tools for background detection and correction are modulation of sources, modulation of the magnetic field, and modulation of the states or directions of the polarizers with respect to each other or to the magnetic field. Thus, improved techniques of graphite furnace solid sampling, in combination with CFS signal generation and background correction, are regarded with hopeful perspectives.

F. Resolution of Isotope Structures

A very interesting perspective has been shown by Stephens.[80] A CFS apparatus in Voigt configuration is used, the polarizer under an angle of 45° with respect to the magnetic field, but with the analyzer perpendicular to the field and an additional modulated phase retarder inserted between the sample and analyzer under an angle of 45° to the field. Thus, the state of analyzed polarization is modulated with the frequency f, being alternately in a state of eliptical polarization with a predominantly left- and right-hand circular component. The amplitudes of the frequencies f and 2f of the transmitted intensity are detected by lock-in systems.

As shown in the work of reference, the fundamental amplitude A(f) of the frequency f in proportional to the dispersive real part $\Delta n'$ of the plasma-birefringence function at the wavelength of the source line, while the first harmonic A(2f) is proportional to the dichroic imaginary part $\Delta n''$. The ratio $S = A(f)/A(2f) \approx \Delta n'/\Delta n''$ is almost independent from the concentration, but it depends very sensitively on the isotopic composition, since dichroism may go through zero and change its sign at a certain magnetic field strength. Without need of nonstandard sources or atomizers, changes of contents of Pb208 in natural lead from 52 to 53% could be detected. Measurements with approches of Zeeman scanning in an ETA-ZAAS apparatus have been also carried out with a low-pressure atomizer.[104]

G. Costs

The costs are evidently to be compared with a ZAAS spectrometer. Additional costs for a CFS spectrometer result from the polarizer-analyzer system; a pair of high-quality Glan-Taylor or Rochon prisms will cost between $3000 and $8000. By reflective configurations, one polarizer can be spared. Due to the low number of lines of the pure resonance spectrum, CFS does not need a spectrograph with a very high resolving power. This favorable feature spares a lot of costs compared with an emission spectrometer. As for AAS, an instrument of typically 10 to 25 cm focal length will be satisfactory.

Costs of light sources will be reduced by the reduced number and the increased lifetime of the required sources. However, the power supply for a 450-W Xe lamp will be more expensive than for a 20-W hollow-cathode lamp. Related to the reduced intensity of the

zero method, sensitive detection and digital conversion by photon counting will be available without very costly efforts.

Consequently, costs of instruments for ZAAS or CFS will be generally of the same order of magnitude. An instrument with flame atomization, which is outlined for operation with combined approaches of ZAAS, OES, and CFS, will not need much higher hardware costs than a ZAA spectrometer. Furthermore, the multielement capability spares not only time of operation, but also material such as furnace tubes and supply of sheath gases cooling water and energy. An apparatus that has been designed as a low-cost instrument for sequential operation in combination with flame atomization has been specially constructed for purposes of water analysis in drinking-water supply. It works with a 12.5-cm monochromator in combination with a photomultiplier and can be equipped with Xe sources of 75 to 450 W.

IX. SUMMARY

The properties and perspectives of CFS are summarized as follows:

1. Excitation-independent atomization, atomization-independent probing
   Atomization by graphite furnaces, flames, plasmas
   Probing by continuum sources and line sources
2. Real multielement capability with continuum sources
   Simultaneous or sequential multielement determination
   Improved speed, promptness, and versatility
   Reduced number of required sources
   Sparing of time
   Sparing of furnace cuvettes, sheath gas, and energy
3. Atomic resonance interaction line spectrum
   Multielement determination with low spectral resolving power
   Low line density, easy line classification
   Weak spectral interferences
   Suitability of position-sensitive detectors and diode arrays
4. Zero method
   Direct optical signal generation
   Unspecific absorption interferes only with the signal intensity
   Enables real time-resolved detection
5. Square-law sensitivity
   Optical expansion of the analytical signal
   Analytical compression of spectral interferences and background
   High time resolution
6. Usability of xenon lamps
   Unproblematic long-life source
   Reduction of the number of required sources
   Full suitability for line sources
   Nondispersive multielement determination with line sources
7. Flexibility and versatility
   Compatibility with ZAAS and OES
   Option of combined detection modes
   Suitable for computer-controlled, computer-optimized operation
8. Favorable inherent background features
   Zero method
   Square-law expanded detection, high specific sensitivity
   Mainly unstructured spectral background with continuum sources

9. Additional capability for background detection and correction
   Suited for detection and correction of spectral interferences
   Suited for detection and correction of unspecific absorption
   Suited for direct solid sampling
10. Special applications
   Isotope determination
   Measurement of optical line widths, hyperfine structures, isotope shifts

ACKNOWLEDGMENTS

The author is indebted to the Bundesminister für Forschung und Technologie (BMFT) for financial support. Thanks are furthermore expressed to H. Bedenbender, H. Debus, M. Gross, and Dr. G. Lasnitschka for helpful discussions and advice; to J. Purder and D. Spengler for a lot of valuable technical help; and to A. Cramer and W. Grimm for assistance with the word processor.

REFERENCES

1. **Corney, A., Kibble, B. P., and Series, G. W.,** *Proc. R. Soc.*, A293, 70, 1966.
2. **Hanle, W.,** *Z. Phys.*, 30, 93, 1924.
3. **Hermann, A., Meyenn, K. V., and von Weisskopf, V.,** Wolfgang Pauli, scientific correspondence with Bohr, Einstein, Heisenberg u.a., in *Sources in the History of Mathematical and Physical Sciences*, Vol. 1, Klein, M. J. and Toomer, G. J., Eds., Springer-Verlag, Berlin, 1979.

3a. **Kastler, A.,** *Phys. Bl.*, 30, 394, 1974.

4. **Hanle, W.,** *Oberhess. Naturwiss. Zeitschr.*, 48, 57, 1984.
5. **Hackett, R. Q. and Series, G. W.,** *Opt. Commun.*, 2, 93, 1970.
6. **Durrant, A. V. and Landheer, B.,** *J. Phys.*, B4, 1200, 1971.
7. **Stanzel, G.,** *Phys. Lett.*, 47A, 283, 1974.
8. **Siegmund, W. and Scharmann, A.,** *Z. Phys.*, A276, 19, 1976.
9. **Church, D. A. and Hadeishi, T.,** *Phys. Rev.*, A8, 1864, 1973.
10. **Stanzel, G.,** *Phys. Lett.*, 41A, 335, 1974.
11. **Hanle, W. and Stanzel, G.,** *Z. Naturforsch.*, 25A, 309, 1970.
12. **Hanle, W., Scharmann, A., Schnaas, N., and Siegmund, W.,** *Phys. Lett.*, 49A, 277, 1974.
13. **Demtröder, W.,** *Grundlagen und Techniken der Laserspektroskopie*, Springer-Verlag, New York, 1977.
14. **Gawlik, W. and Series, G. W.,** *Springer Ser. Opt. Sci.*, 21, 210, 1979.
15. **Giraud-Cotton, S., Kaftandjian, V. P., and Klein, L.,** *Phys. Lett.*, 88A, 453, 1982.
16. **Brand, H., Drake, K.-H., Lange, W., and Mlynek, J.,** *Phys. Lett.*, 75A, 345, 1980.
17. **Hermann, G. and Scharmann, A.,** *Z. Phys.*, 254, 46, 1972.
18. **Bitter, F., Plotkin, H., Richter, B., Teriotdale, A., and Young, J. F. R.,** *Phys. Rev.*, 91, 421, 1953.
19. **Bitter, F., Davis, S. P., Richter, B., and Young, J. F. R.,** *Phys. Rev.*, 96, 1531, 1954.
20. **Bitter, F.,** *Appl. Opt.*, 1, 1, 1962.
21. **Hadeishi, T.,** *Appl. Phys. Lett.*, 21, 438, 1972.
22. **Fernandez, F. J., Myers, S. A., and Slavin, W.,** *Anal. Chem.*, 52, 741, 1980.
23. **Church, D. A., Hadeishi, T., McLaughlin, R. D., and Zak, B. D.,** Lawrence Berkeley Laboratory Preprint LBL-1781.

23a. **Hadeishi, T.,** Lecture Notes at University of Aarhus, Denmark, 1973.

24. **Church, D. A. and Hadeishi, T.,** *Appl. Phys. Lett.*, 24, 185, 1974.
25. **Ito, M., Murayama, S., Kayama, K., and Yamamoto, M.,** *Spectrochim. Acta*, 32B, 347, 1977.
26. **Ito, M.,** *Anal. Chem.*, 52, 1592, 1980.
27. **Yamamoto, M. and Murayama, S.,** *J. Opt. Soc. Am.*, 69, 781, 1979.
28. **Debus, H., Hanle, W., Scharmann, A., and Wirz, P.,** *Spectrochim. Acta*, 36B, 1015, 1981.
29. **Debus, H., Ganz, S., Gross, M., Hermann, G., and Scharmann, A.,** *Laser Optoelektron.*, 17, 123, 1985.

30. **Ottaway, J. M. and Shaw, F.,** *Analyst,* 100, 438, 1975.
31. **Falk, H.,** *CRC Crit. Rev. Anal. Chem.,* in press.
32. **Harnly, J., O'Haver, T. C., Golden, B., and Wolf, W. R.,** *Anal. Chem.,* 51, 2007, 1979.
32a. **Harnly, J. M., Miller-Ihli, N. J., and O'Haver, T. C.,** *Spectrochim. Acta,* 39B, 305, 1984.
33. **O'Haver, T. C., Harnly, J. M., Marshall, L., Caroll, J., Littlejohn, D., and Otaway, J. M.,** *Analyst,* 110, 451, 1985.
34. **Wirz, P., Debus, H., Hanle, W., and Scharmann, A.,** *Spectrochim. Acta,* 37B, 1013, 1982.
35. **Kankare, J. J. and Stephens, R.,** *Spectrochim. Acta,* 35B, 849, 1980.
36. **Yamamoto, M., Murayama, S., Ito, M., and Yasuda, M.,** *Spectrochim. Acta,* 35B, 43, 1980.
37. **Condon, E. U. and Shortley, G. H.,** *The Theory of Atomic Spectra,* Cambridge University Press, Cambridge, 1967.
38. **Brink, D. M. and Satchler, G. R.,** *Angular Momentum,* Clarendon Press, Oxford, 1968.
39. **Born, M.,** *Optik,* Springer-Verlag, Berlin, 1933.
40. **Fried, B. D. and Conte, S. D.,** *The Plasma Dispersion Function,* Academic Press, London, 1961.
41. **Loudon, R.,** *The Quantum Theory of Light,* Clarendon Press, Oxford, 1973.
42. **Kankare, J. J. and Stephens, R.,** *Appl. Spectrosc.,* 34, 590, 1980.
43. **Gross, M., Hermann, G., and Scharmann, A.,** in press.
44. **Debus, H., Gross, M., Hermann, G., Scharmann, A., and Seib, M.,** *Analytiktreffen,* Neubrandenburg, 1986.
45. **Church, D. A., Hadeishi, T., McLaughlin, R. D., and Zak, B. D.,** *Natl. Meet. Div. Environ. Chem. Am. Chem. Soc.,* 13, 47, 1973.
46. **Kitagawa, K., Shigeyasu, T., and Takeuchi, T.,** *Analyst,* 103, 1021, 1978.
47. **Debus, H., Hermann, G., and Scharmann, A.,** in press.
48. **Kersey, A. D. and Dawson, J. D.,** *Anal. Proc. R. Soc. Chem.,* 18, 187, 1981.
49. **Hirokawa, K.,** *Fresenius Z. Anal. Chem.,* 324, 612, 1986.
50. **Durrant, A. V.,** *J. Phys.,* B5, 133, 1972.
51. **Kitagawa, K., Shigeyasu, T., and Takeuchi, T.,** *Spectrochim. Acta,* 34B, 389, 1979.
52. **Kitagawa, K., Aot, N., and Tsuge, S.,** *Spectrochim. Acta,* 36B, 1097, 1981.
53. **Welz, B.,** *Atomabsorptionsspektrometrie,* Verlag Chemie, Weinheim, 1983.
54. **Massmann, H.,** *Fresenius Z. Anal. Chem.,* 225, 203, 1967.
55. **L'vov, B. V.,** *Spectrochim. Acta,* 17, 761, 1961.
56. **Frech, W. and Cedergren, A.,** *Prog. Anal. Atom. Spectrosc.,* 3, 279, 1980.
57. **van den Broek, W. M. G. T. and de Galan, L.,** *Anal. Chem.,* 49, 2176, 1977.
58. **Sturgeon, R. E. and Chakrabarti, C. L.,** *Prog. Anal. Atom. Spectrosc.,* 1, 5, 1978.
59. **Eklund, R. H. and Holcombe, A. J.,** *Anal. Chim. Acta,* 109, 97, 1979.
60. **Chakrabarti, C. L., Wan, C. C., Hamed, H. A., and Bertels, P. C.,** *Anal. Chem.,* 53, 444, 1981.
61. **L'vov, B. V., Pelieva, L. A., and Sharnopolsky, A. I.,** *Zh. Prikl. Spektrosk.,* 27, 395, 1977.
62. **Debus, H., Gross, M., Hermann, G., and Scharmann, A.,** 2nd Int. Colloq. *Solid Sampling with Atomic Spectroscopic Methods,* Wetzlar, 1986.
63. **Takada, K. and Hirokawa, K.,** *Spectrochim. Acta,* 39B, 1113 1984.
64. **Hermann, G., Krüger, R., Scharmann, A., and Seib, M.,** in press.
65. **Kitagawa, K., Suzuki, M., Aoi, N., and Tsuge, S.,** *Spectrochim. Acta,* 36B, 21, 1981.
66. **Kersey, A. D., Dawson, J. B., and Ellis, D. J.,** *Spectrochim. Acta,* 35B, 865, 1980.
67. **Walsh, A.,** *Anal. Proc.,* 21, 54, 1984.
68. **Kitagawa, K., Nanya, T., and Tsuge, S.,** *Spectrochim. Acta,* 36B, 9, 1981.
69. **Murayama, S., Yasuda, M., Ito, M., Oishi, K., and Yamamoto, M.,** *Spectrochim. Acta,* 35B, 159, 1979.
70. **Hirokawa, K. and Namiki, M.,** *Spectrochim. Acta,* 37B, 165, 1982.
71. **Ganz, S., Gross, M., Hanle, W., Hermann, G., and Sharmann, A.,** *Instrumentelle Multi-Element-Analyse,* Sansoni, B., Ed., VCH Verlagsgesellschaft GmbH, Weinheim, 1985, 385.
72. **Hanle, W., Scharmann, A., and Wirz, P.,** *Phys. Lett.,* 69A, 12, 1978.
73. **Gurvinder, S. and Stephens, R.,** *Spectrochim. Acta,* 39B, 335, 1983.
74. **Hirokawa, K., Namiki, M., and Saase, M.,** *Fresenius Z. Anal. Chem.,* 313, 561, 1982.
75. **Hirokawa, K.,** *Anal. Chem.,* 52, 1967, 1980.
76. **Hirokawa, K. and Namiki, M.,** *Spectrochim. Acta,* 36B, 649, 1981.
77. **Debus, H., Ganz, S., Hanle, W., Hermann, G., and Scharmann, A.,** *Instrumentelle Multi-Element-Analyse,* Sansoni, B., Ed., VCH Verlagsgesellschaft mbH, Weinheim, 1985, 391.
78. **Namiki, M. and Hirokawa, K.,** *Fresenius Z. Anal. Chem.,* 316, 795, 1983.
79. **Hirokawa, K. and Kimura, J.,** *Fresenius Z. Anal. Chem.,* 325, 396, 1986.
80. **Stephens, R.,** *Spectrochim. Acta,* 40B, 1259, 1985.
81. **Gross, M., Ganz, S., Hermann, G., and Scharmann, A.,** Colloquium Spectroscopicum Internationale XXIV (CSI), Garmisch-Partenkirchen, 1985, 326.

82. **Bedenbender, H., Hermann, G., and Scharmann, A.,** *Spiegel der Forschung*, Wissenschaftsmagazin der Justus-Liebig-Universität, Giessen, 1987.
83. **Hermann, G., Scharmann, A. et al.,** *Exposition Prospect Hannover-Messe 1987*, Justus-Liebig-Universität, Giessen, 1987.
83a. **Bedenbender, H. and Cramer, A. et al.,** *Hessische Hochschulen*, University Contributions on Hannover-Messe, 1987.
84. **Broekaert, J. A. C.,** *Spectrochim. Acta*, 37B, 65, 1982.
85. **Gross, M., Hermann, G., and Scharmann, A.,** in press.
86. **Gross, M.,** Das Spektrale Profil der Kohaerenten Optischen Vorwaertsstreuung und sein Einfluss auf die Quantitative Elementanalyse, thesis, Justus-Liebig-Universität, Griessen, 1987.
87. **Demtröder, W.,** *Laser Spectroscopy*, Springer Ser. Chem. Phys. 5, Springer-Verlag, New York, 1981.
88. **Stephens, R.,** *Spectrochim. Acta*, 38B, 1077, 1983.
89. **Stephens, R. and Kankare, J. J.,** *Spectrochim. Acta*, 38B, 1301, 1983.
90. **Stephens, R.,** *Anal. Chim. Acta*, 98, 291, 1978.
91. **Hermann, G. et al.,** in press.
92. **Debus, H., Hermann, G., and Scharmann, A.,** *Fresenius Z. Anal. Chem.*, 323, 767, 1986.
93. **Debus, H., Gross, M., Hermann, G., Lasnitschka, G., and Scharmann, A.,** *Fresenius Z. Anal. Chem.*, in press.
94. **Debus, H.,** Untersuchungen Über die Anwendung der Kohaerenten Optischen Vorwaertsstreuung zur Simultanen Multielemtanalyse, thesis, Justus-Liebig-Universität, Giessen, 1987.
95. **Kitagawa, K., Koyama, T., and Takeuchi, T.,** *Analyst*, 104, 822, 1979.
96. **Debus, H., Hermann, G., and Scharmann, A.,** *Post CSI Sumposium* , Meersburg, 1985.
97. **Debus, H., Ganz, S., Hermann, G., and Scharmann, A.,** Colloquium Spectroscopicum Internationale (CSI), Garmisch-Partenkirchen, 1985, 328.
98. **Gurvinder, S., Jolly, G., and Stephens, R.,** *Spectrochim. Acta*, 39B, 335, 1984.
99. **Davis, L. A. and Winefordner, J. D.,** *Anal. Chem.*, 59, 309, 1987.
100. **Fuller, C. W.,** *Electrothermal Atomization for Atomic Absorption Spectrometry*, Anal. Sci. Monogr. 4, The Chemical Society Burlington House, London, 1977.
101. **Boumans, P. W. J. M.,** *Fresenius Z. Anal. Chem.*, 324, 397, 1986.
102. **Hadeishi, T. and McLaughlin, R.,** *Fresenius Z. Anal. Chem.*, 322, 657, 1985.
103. **Langmyhr, F. J.,** *Fresenius Z. Anal. Chem.*, 322, 654, 1985.
104. **Deninger, R., Ganz, S., Grimm, W., Hermann, G., and Scharmann, A.,** *Prog. Anal. Spectrosc.*, 10, 335, 1987.